Draft version October 15, 2019
Typeset using LaTeX **twocolumn** style in AASTeX62

arXiv:1910.03410v2 [astro-ph.HE] 14 Oct 2019

Carnegie Supernova Project-II: Near-infrared Spectroscopic Diversity of Type II Supernovae*

S. Davis,[1] E. Y. Hsiao,[1] C. Ashall,[1] P. Hoeflich,[1] M. M. Phillips,[2,3] G. H. Marion,[4] R. P. Kirshner,[5,6] N. Morrell,[2] D. J. Sand,[7] C. Burns,[8] C. Contreras ,[2] M. Stritzinger ,[9] J. P. Anderson,[10] E. Baron,[9,11,12] T. Diamond,[13] C. P. Gutiérrez,[14] M. Hamuy,[15] S. Holmbo,[9] M. M. Kasliwal,[16] K. Krisciunas ,[17] S. Kumar,[1] J. Lu,[1] P.J. Pessi,[18,19] A. L. Piro,[20] J. L. Prieto,[21] M. Shahbandeh,[1] and N. B. Suntzeff[17]

[1] *Department of Physics, Florida State University, 77 Chieftan Way, Tallahassee, FL 32306, USA*
[2] *Carnegie Observatories, Las Campanas Observatory, Casilla 601, La Serena, Chile*
[3] *Wyatt-Green Preeminent Visiting Scholar of the Department of Physics, Florida State University*
[4] *University of Texas at Austin, 1 University Station C1400, Austin, TX, 78712-0259, USA*
[5] *Gordon and Betty Moore Foundation, 1661 Page Mill Road, Palo Alto, CA 94304*
[6] *Harvard-Smithsonian Center for Astrophysics, 60 Garden Street, Cambridge, MA 02138*
[7] *Department of Astronomy/Steward Observatory, 933 North Cherry Avenue, Rm. N204, Tucson, AZ 85721-0065, USA*
[8] *Observatories of the Carnegie Institution for Science, 813 Santa Barbara St., Pasadena, CA 91101, USA*
[9] *Department of Physics and Astronomy, Aarhus University, Ny Munkegade 120, DK-8000 Aarhus C, Denmark*
[10] *European Southern Observatory, Alonso de Córdova 3107, Casilla 19, Santiago, Chile*
[11] *Homer L. Dodge Department of Physics and Astronomy, University of Oklahoma, 440 W. Brooks, Rm 100, Norman, OK 73019-2061, USA*
[12] *Hamburger Sternwarte, Gojenbergsweg 112, D-21029 Hamburg, Germany*
[13] *NASA Goddard Space Flight Center, Greenbelt, MD 20771, USA*
[14] *Department of Physics and Astronomy, University of Southampton, Southampton, SO17 1BJ, UK*
[15] *Departamento de Astronomía, Universidad de Chile, Casilla 36-D, Santiago, Chile*
[16] *4Division of Physics, Mathematics and Astronomy, California Institute of Technology, Pasadena, California 91125, USA*
[17] *George P. and Cynthia Woods Mitchell Institute for Fundamental Physics & Astronomy, Texas A&M University, Department of Physics, 4242 TAMU, College Station, TX 77843*
[18] *Instituto de Astrofísica de La Plata (IALP), CONICET, Paseo del bosque S/N, 1900, Argentina*
[19] *Facultad de Ciencias Astronómicas y Geofísicas (FCAG), Universidad Nacional de La Plata (UNLP), Paseo del bosque S/N, 1900, Argentina.*
[20] *Observatories of the Carnegie Institution for Science, 813 Santa Barbara St, Pasadena, CA 91101, USA*
[21] *Núcleo de Astronomía, Facultad de Ingeniería y Ciencias, Universidad Diego Portales, Ejército 441, Santiago, Chile*

(Accepted October 7, 2019)

Submitted to ApJ

ABSTRACT

We present 81 near-infrared (NIR) spectra of 30 Type II supernovae (SNe II) from the *Carnegie Supernova Project-II* (CSP-II), the largest such dataset published to date. We identify a number of NIR features and characterize their evolution over time. The NIR spectroscopic properties of SNe II fall into two distinct groups. This classification is first based on the strength of the He I $\lambda 1.083\,\mu$m absorption during the plateau phase; SNe II are either significantly above (spectroscopically *strong*) or below 50 Å (spectroscopically *weak*) in pseudo equivalent width. However between the two groups, other properties, such as the timing of CO formation and the presence of Sr II, are also observed. Most surprisingly, the distinct *weak* and *strong* NIR spectroscopic classes correspond to SNe II with slow and fast declining light curves, respectively. These two photometric groups match the modern nomenclature of SNe IIP and IIL. Including NIR spectra previously published, 18 out of 19 SNe II follow this slow declining-spectroscopically *weak* and fast declining-spectroscopically *strong* correspondence. This is

Corresponding author: Scott Davis
sfd15b@my.fsu.edu

* This paper includes data gathered with the 6.5 meter *Magellan* Telescopes at Las Campanas Observatory, Chile.

in apparent contradiction to the recent findings in the optical that slow and fast decliners show a continuous distribution of properties. The *weak* SNe II show a high-velocity component of helium that may be caused by a thermal excitation from a reverse-shock created by the outer ejecta interacting with the red supergiant wind, but the origin of the observed dichotomy is not understood. Further studies are crucial in determining whether the apparent differences in the NIR are due to distinct physical processes or a gap in the current data set.

Keywords: supernova, near-infrared, spectroscopy

1. INTRODUCTION

Type II supernovae (SNe II) are classified by the presence of Balmer-series hydrogen lines in their optical spectra (Minkowski 1941). They are believed to result from the explosion of massive stars ($> 8M_{\odot}$) that have retained a significant portion of their hydrogen envelope. Pre-explosion images of SN II locations suggest that the majority of SNe II are the result of red supergiant (RSG) explosions (e.g. Smartt et al. 2004; Maund et al. 2005; Smartt 2009, 2015; Van Dyk 2017; Van Dyk et al. 2019).

Historically, SNe II have been divided into subclasses based on the shape of their light curves (Barbon et al. 1979). In this work the more modern nomenclature for SNe II photometric classifications is used, with SNe exhibiting fast declining light curves classified as SNe IIL, and those with slow declining light curves classified as SNe IIP. The majority of SN II V-band light curves evolve with an initial rise to maximum followed by a steep decline before settling onto a more gentle decline, commonly referred to as the plateau. During this plateau phase, hydrogen recombination drives the light curve until a sharp decline onto the radioactive tail (Woosley, & Iben 1987). One photometric and two spectroscopic classes were added within the SN II population: SNe IIb, SNe IIn, and SN 1987A-like, respectively (Arnett et al. 1989; Schlegel 1990; Filippenko et al. 1993). For the remainder of this paper, we will use the SNe II designation to refer to the collection of SNe that previously have been classified as SNe IIL or SNe IIP as the other previously mentioned sub-types (IIb, IIn, and SN 1987A-like) are not included in the data analyzed.

It has been suggested that fast-declining SNe II have a smaller amount of hydrogen in their envelopes than slow-declining SNe II (Popov 1993; Faran et al. 2014; Gutiérrez et al. 2014; Moriya et al. 2016). However, it is still not known whether there are progenitor differences of explosion scenarios that separate the slow and fast declining SNe II into two distinct groups (Barbon et al. 1979; Patat et al. 1993). Furthermore, recent publications have shown that there is no discrete photometric separation between these SNe (e.g. Anderson et al. 2014; Sanders et al. 2015; Valenti et al. 2016; Galbany et al. 2016; Pessi et al. 2019); although see Arcavi et al. (2012) for a possible separation.

The amount of SN II optical data obtained has greatly increased in the past decade with the focus turning towards larger samples to examine their spectroscopic and photometric diversity (Anderson et al. 2014; Faran et al. 2014; Gutiérrez et al. 2014; Valenti et al. 2016; Galbany et al. 2016; Rubin, & Gal-Yam 2016; Gutiérrez et al. 2017a,b; Faran et al. 2018). Large photometric studies have defined parameters useful for characterizing the diversity of SN II optical light curves. They found that brighter SNe II decline more quickly at every phase, have shorter plateau phases, and higher ^{56}Ni masses. This is significant because it further supports that faster declining SNe II are the result of explosions with lower hydrogen envelope masses, which causes their shorter plateau duration. Gutiérrez et al. (2017a), using optical spectra, found that SNe II span a continuous range in equivalent widths and velocities.

SNe II in the NIR have yet to be explored in detail. However, there are well-known advantages to observing spectroscopically in the NIR, namely, the variety of strong lines present, less line blending when compared to the optical, and a lower optical depth revealing the core at earlier times (Meikle et al. 1993). Furthermore, at late times, carbon monoxide (CO) is sometimes observed (Spyromilio et al. 1988, 2001; Rho et al. 2018).

Spectroscopically, the most well-studied SN II in the NIR is SN 1987A (Bouchet et al. 1987; Oliva et al. 1987; Catchpole et al. 1988; Elias et al. 1988; Rank et al. 1988; Whitelock et al. 1988; Catchpole et al. 1989; Meikle et al. 1989; Sharp, & Hoeflich 1990; Bouchet et al. 1991; Danziger et al. 1991; Meikle et al. 1991, 1993) with over 30 NIR spectra of SN 1987A available. SN 1987A exploded in the Large Magellanic Cloud, which allowed for extensive spectroscopic and photometric coverage still being obtained today. SN 1987A was a peculiar SN II, that most likely originated from a blue supergiant progenitor (Podsiadlowski 1992). This peculiarity led to the definition of an additional SN II subclass, SN 1987A-like, which are SNe that have long rising light curves.

Most previously published SNe II NIR spectra are of a single SN across a small number of epochs (Benetti et al.

2001; Hamuy et al. 2001; Elmhamdi et al. 2003; Pozzo et al. 2006; Pastorello et al. 2009; Maguire et al. 2010; Fraser et al. 2011; Tomasella et al. 2013; Morokuma et al. 2014; Dall'Ora et al. 2014; Jerkstrand et al. 2014; Takáts et al. 2014, 2015; Valenti et al. 2015, 2016; Rho et al. 2018; Bostroem et al. 2019; Szalai et al. 2019). These works have been able to characterize the general spectral line evolution from a couple days past explosion through the nebular phase. The SN IIP SN 1999em was particularly well studied allowing line identification and analysis (Hamuy et al. 2001; Elmhamdi et al. 2003), however, SNe II are diverse and thus SNe II in the NIR have not been fully explored.

By modeling the NIR and optical spectra of SNe II, Takáts et al. (2014) found that the $0.98-1.12\,\mu$m region contains a high-velocity (HV) helium feature on the blue side of the Paschen gamma (P_γ) hydrogen absorption. This feature, previously unconfirmed, mirrors the velocity of the HV hydrogen feature claimed in the optical by Gutiérrez et al. (2017a).

In this paper we present the largest SNe II NIR dataset published to date. The data were obtained between 2011 to 2015 as a part of the *Carnegie Supernova Project-II* (CSP-II, e.g. Phillips et al. 2019); CSP-II was an NSF-supported program to study Type Ia SNe as distance indicators, that aimed to improve upon CSP-I (Hamuy et al. 2006) by observing objects from untargeted searches detected in the Hubble flow. CSP-II also worked to obtain a large sample of SN Ia NIR spectra for studies in cosmology and in their explosion physics (Hsiao et al. 2019). Furthermore, NIR spectra of all types of nearby SNe were obtained as the current sample is small and they are crucial for understanding the origins of these explosions.

The sections of this paper are outlined as follows. Section 2 is an overview of the data sample, including the observation and reduction techniques used. In Section 3, we describe the process used for measuring various photometric and spectroscopic properties. In Section 4, we outline the NIR spectral features and their evolution over time. In Section 5, properties of the NIR hydrogen features are discussed. Section 6 describes the observed NIR spectral dichotomy. In Section 7, we present the results of a principal component analysis (PCA) on the CSP-II SNe II dataset and corresponding NIR spectral templates. The discussion of results and conclusions are in Sections 8 and 9, respectively.

2. OBSERVATIONS AND SAMPLE

The CSP-II sample contains 92 NIR spectra of 32 SNe II. Figure 1 shows the phase of each NIR spectrum, as well as the distribution of number of spectra taken per SN. NIR spectra were obtained with the Magellan Baade Telescope, equipped with the Folded-port Infrared Echellette (FIRE; Simcoe et al. 2013), and with the NASA Infrared Telescope Facility (IRTF), equipped with SpeX (Rayner et al. 2003). The spectra were reduced and corrected for telluric absorption following the procedures outlined in Hsiao et al. (2019). Spectra obtained after 300 days are not included in this sample because they are well into the nebular phase, giving a total of 81 NIR spectra from 30 SNe II. See Table 1 for a list of all SNe used, Table 2 for a log of the observations, and Figures 2-4 for all the spectroscopic data. Spectra can be downloaded from the Web. [1] The high throughput of FIRE allows us to recover enough counts in the telluric regions to enable telluric corrections, such as the Pα feature, to a precision of 10% or better in 70% of our sample. Eleven SNe II have multi-epoch observations, and 14 have well-sampled light curves. Photometry was obtained with the Las Campanas Observatory Swope and du Pont telescopes. The observing strategy and technique for the photometric data are described in Phillips et al. (2019).

The sample ranges from redshift 0.002 to 0.037, with a mean of 0.013 and median of 0.009. Table 3 lists the redshift and host galaxy for each SN II within the sample. Host information obtained from the NASA/IPAC Extragalactic Database (NED)[2], provides us with distance estimates to each SN II. Table 4 lists both redshift-independent and redshift-dependent distances. We use the redshift-independent distance to calculate absolute luminosity whenever possible. Our sample contains no SNe IIn, SNe IIb, or SN 1987A-like objects.

For each SN II, the explosion date is assumed to be the midpoint between the last non-detection and discovery, while the uncertainty in the explosion date is taken as half of the range between last non-detection and the discovery date, a method adopted by Anderson et al. (2014); Gutiérrez et al. (2017a). Spectral matching techniques are employed in order to constrain the explosion date using the Supernova Identification (SNID) code for each SN in the sample, even those with a well constrained, less than 20 days before discovery, last non-detection (Blondin, & Tonry 2007). The phases obtained using SNID matches those from the last non-detection method, without any obvious bias toward last non-detection or discovery. It is assumed that there is a flat prior in the phase distribution. SNID does not have NIR templates, so all spectral matching was done

[1] https://csp.obs.carnegiescience.edu/data
[2] http://ned.ipac.caltech.edu

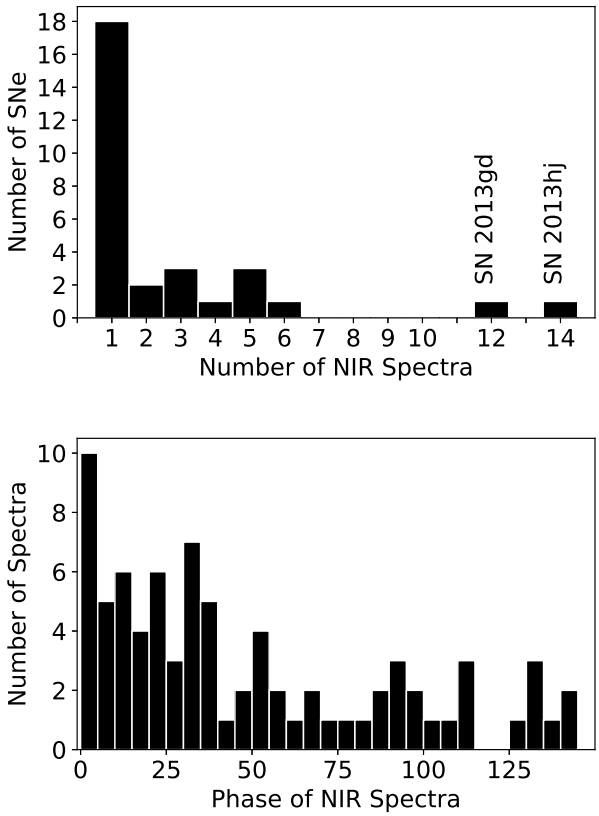

Figure 1. Number of SNe II with time-series observations (top panel), and number of NIR spectra at each epoch relative to explosion date (bottom panel). We do not consider nebular phase spectra in this work.

in the optical with previously published data. Using SNID with updated SN II templates has been shown to be a valid method to constrain the explosion epoch (e.g. Anderson et al. 2014; Gutiérrez et al. 2017a). When using SNID, the explosion date is taken as the average of the best matched spectra and the range is taken as the error. Of the 30 SNe II, 13 have well-defined last non-detections, 8 have explosion dates constrained with SNID, 4 have poorly constrained last non-detections, and 5 have no optical data and no available last non-detection date.

3. MEASUREMENTS

3.1. *Photometric measurements*

Photometry is a valuable tool in characterizing SNe II, allowing for comparisons between photometric and spectral properties. V-band light curves have become the standard in measuring photometric properties of SNe II (e.g. Anderson et al. 2014; Valenti et al. 2016; Gutiérrez et al. 2017b). We follow the methods of Anderson et al. (2014) and Faran et al. (2014) for parameterizing the V-band light curves of SNe II. For each light curve we attempt to measure s_1, s_2, s_3, $M_{\rm max}$, $M_{\rm end}$, $M_{\rm tail}$, t_0, $t_{\rm tran}$, $t_{\rm end}$, and $t_{\rm PT}$. Further discussion of the fitting techniques used can be found in Appendix A.

For our sample we use a cutoff of $s_2 = 1.4$ mag per 100 days, where s_2 is the slope of the SN light curve during the plateau phase, for the separation between slow and fast declining SNe II. This number was chosen as it follows the division used in the literature to separate the IIP and IIL classes (Dall'Ora et al. 2014; Valenti et al. 2015, 2016; Bose et al. 2016). It has been shown that there is no clear distinction between slow and fast declining SNe II when looking at the slope of the plateau (Anderson et al. 2014; Gutiérrez et al. 2017b), however, a division has been made for this sample in order to compare spectral properties among the two photometric groups as a possible photometric separation has been seen by Arcavi et al. (2012).

3.2. *Spectroscopic Measurements*

The expansion velocity and pseudo equivalent widths (pEW) of the NIR hydrogen features were measured for each SN II for which photometric properties can be extracted. Both velocity and pEW measurements were performed by Gaussian fits to the absorption and emission features of each P Cygni profile. The region was manually selected for each line. The continuum in the selected region was estimated by a straight line. When fitting a single feature a straight line approximation of the continuum is often adequate. Localized blackbody fits to the same region were prone to over or under estimating the continuum due to contaminating features. Blackbody fits are also inaccurate past $\sim 2\,\mu$m as free-free emission dominates the continuum. The region selected is then flattened by dividing the spectrum by the continuum. The velocity is measured by fitting for the minimum within the selected region. The pEW is measured via the method outlined in Folatelli (2004); Garavini et al. (2007).

Each spectrum used for velocity and pEW measurements has an error spectrum that represents our estimates of the flux measurement error at each pixel. For FIRE observations, the error spectra are the measured dispersion of the flux from mutiple frames at each pixel (Hsiao et al. 2019). For the rest of the observations, the error spectra are estimated by assuming that the Gaussian smoothed (2σ) spectra are the true spectral energy distribution (SED) of the SNe without errors. The flux errors are then taken as the standard deviation from the idealized SED.

A simple Gausssian function is used to fit a feature in order to determine the wavelengths of the feature min-

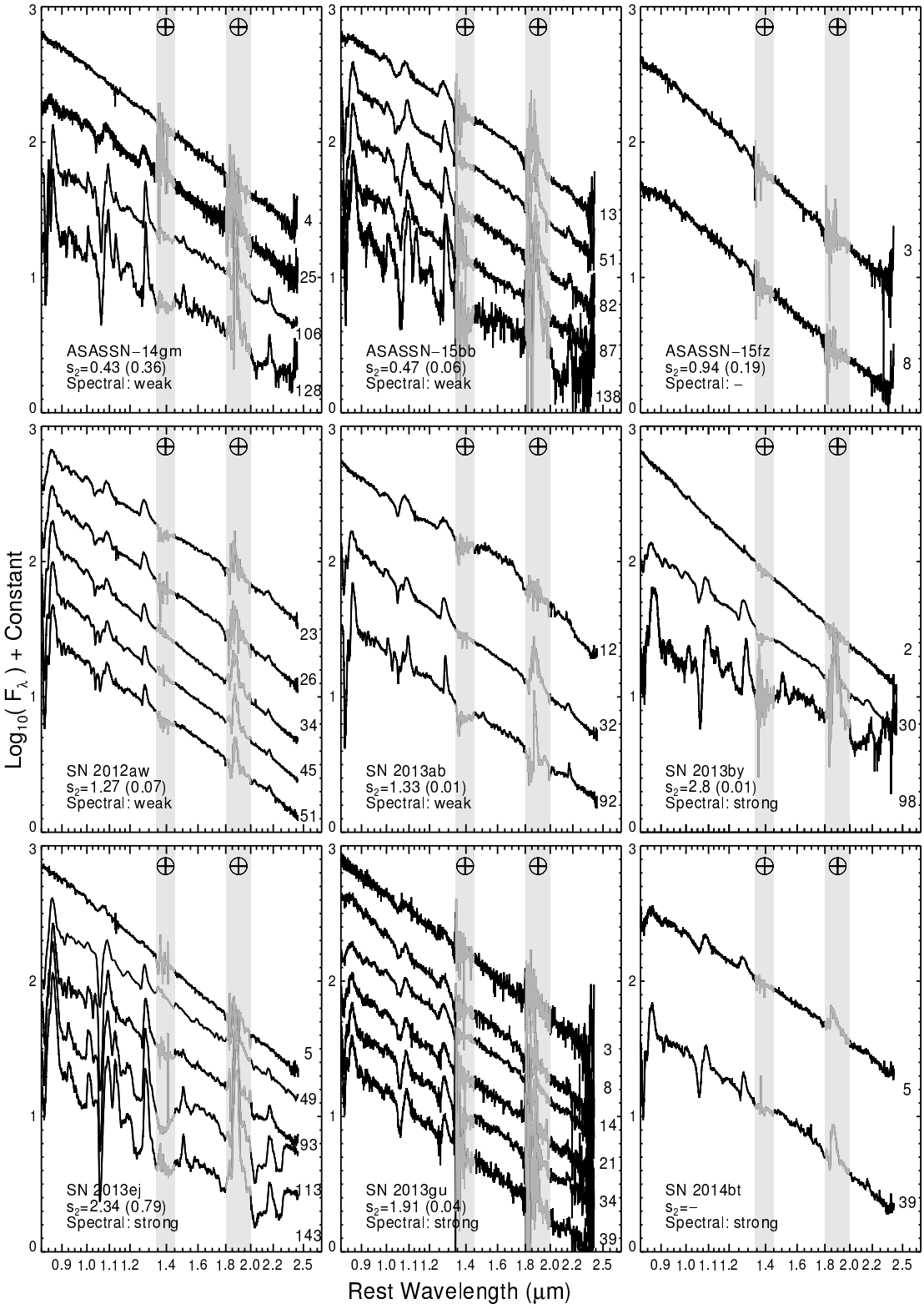

Figure 2. Time evolution for all SNe II with two or more spectra from our sample, excluding SNe 2013gd and 2013hj which are displayed in Figure 3. Grey shaded areas mark wavelengths that have high telluric absorption from the atmosphere. The spectroscopic classification and photometric value s_2 is listed for each SN, with the s_2 error given in parentheses. Days since explosion is provided on the right side of the spectra.

ima and maxima. The resulting reduced χ^2 is smaller than 1 in all fits. This indicates that a Gaussian function is not an accurate representation of the P-Cygni profile shape and perhaps the flux errors were underestimated. However, we consider this method adequate for the purpose of determining the feature extrema. A conservative velocity error is obtained by scaling the Gaussian fit error by the inverse of the reduced χ^2. The diversity in the parent population is not considered in this error.

The pEW of each absorption and emission feature is directly measured by defining a straight-line continuum, and integrating over the enclosed continuum removed area, without assuming any functional form for the shape of the feature. The errors in the measurement of pEW were estimated via Monte Carlo, with realizations generated using the flux error spectra.

4. LINE IDENTIFICATIONS

SNe II as a whole are generally similar spectroscopically in the NIR. Using the spectral line identifications from Branch (1987) and Meikle et al. (1989), we identify the features and evolution over time of the SNe II within our sample; see Figure 5.

4.1. *Early Phase*

Very early time spectra, less than $2-3$ days post explosion, exhibit few spectral lines, as can be seen in the top spectrum of Figure 5, and can be well approximated by a blackbody Rayleigh-Jeans approximation in the NIR. At around 10 days past explosion, the hydrogen Paschen series begins to emerge with P_γ $\lambda1.094\,\mu$m, and P_β $\lambda1.282\,\mu$m the first features seen.

4.2. *Plateau Phase*

As SNe II settle into the plateau phase ~ 20 days past explosion more features appear, see the middle spectrum in Figure 5. The Ca II triplet is the strongest feature at this phase. It initially just shows an absorption feature and develops a stronger P Cygni profile as time passes. It is comprised of a blend of three Ca II lines: two close together and one more prominent, located at $\lambda\lambda0.854\,\mu$m, $0.866\,\mu$m, and $0.892\,\mu$m, respectively. The development of this feature is not uniform, with many SNe II showing different line strengths.

The S I $\lambda0.922\,\mu$m feature shows up in the NIR around 30 days post explosion. The S I P Cygni profile strengthens over time in all SNe II.

Sr II $\lambda1.004$ and $\lambda1.092\,\mu$m are both blended with H I features and cannot be resolved. Sr II $\lambda1.033\,\mu$m appears in all SNe II but with a varied evolution with many SNe not showing Sr II until after the plateau phase ends; however, there are SNe which show strong Sr II absorption from Sr II $\lambda1.033\,\mu$m during the plateau. For these cases, the feature can be seen as early as 20 days past explosion, increasing in strength over time and becoming a dominant feature in the SN spectrum.

P_δ $\lambda1.005\,\mu$m is one of the weaker hydrogen lines detectable in SNe II NIR spectra. Blended with the P_δ feature is Sr II $\lambda1.004\,\mu$m that causes stronger line blending than is seen in the other hydrogen features. The strength of the P Cygni profile does not increase as quickly as other hydrogen features.

P_γ $\lambda1.094\,\mu$m is highly blended with He I $\lambda1.083\,\mu$m and Sr II $\lambda1.092\,\mu$m. It has a very weak absorption, that is only noticeable in most SNe towards the end of the plateau as a notch on the red side of the He I absorption component. The emission in this region is attributed mostly to P_γ and evolves similarly to the other H I features.

During the plateau the most prominent absorption arises from He I $\lambda1.083\,\mu$m and has other possible contributions from Sr II $\lambda1.092\,\mu$m and P_γ $\lambda1.095\,\mu$m. Since other Sr II transitions in this region are weak, it is unlikely that this absorption is dominated by Sr II. He I is excited non-thermally and would only be seen if the ^{56}Ni was located close to the He region in the ejecta (Graham 1988). We note that this feature is not expected to have a significant contribution from H I because no strong H I absorption is present in the other Paschen series lines. However, the emission of this P Cygni profile is most likely to have contribution from P_γ, as strong emission features are seen in other Paschen series lines.

A strong He I absorption profile with a weak emission component is present in the early optical spectra of SNe II (Gutiérrez et al. 2017a). Thus in the NIR, we do not expect He I to contribute a large amount of flux in emission to this feature. It is also possible for the emission component to be shifted blueward by the absorption of H I and Sr II. At 50 days past explosion, this P Cygni profile consists of a blend comprised of He I, H I, and Sr II, with He I $\lambda1.083\,\mu$m being the dominant contributor in absorption. Thus we will refer to this absorption as He I for the remainder of this work. At later times, as the photosphere recedes to the inner hydrogen-rich region, we expect heavier elements to appear. Hence, late contributions from C I and Si I are likely.

Around 50 days post explosion a dichotomy in the region around He I $\lambda1.083\,\mu$m appears. Figure 6 shows two SNe which represent the dichotomy. SNe with more prominent He I absorption show no other lines in this region until later phases when a small absorption, comprised of P_γ and Sr II $\lambda1.092\,\mu$m appears on the red side of the He I absorption. SNe with a shallower He I absorption show other features which are not seen in SNe

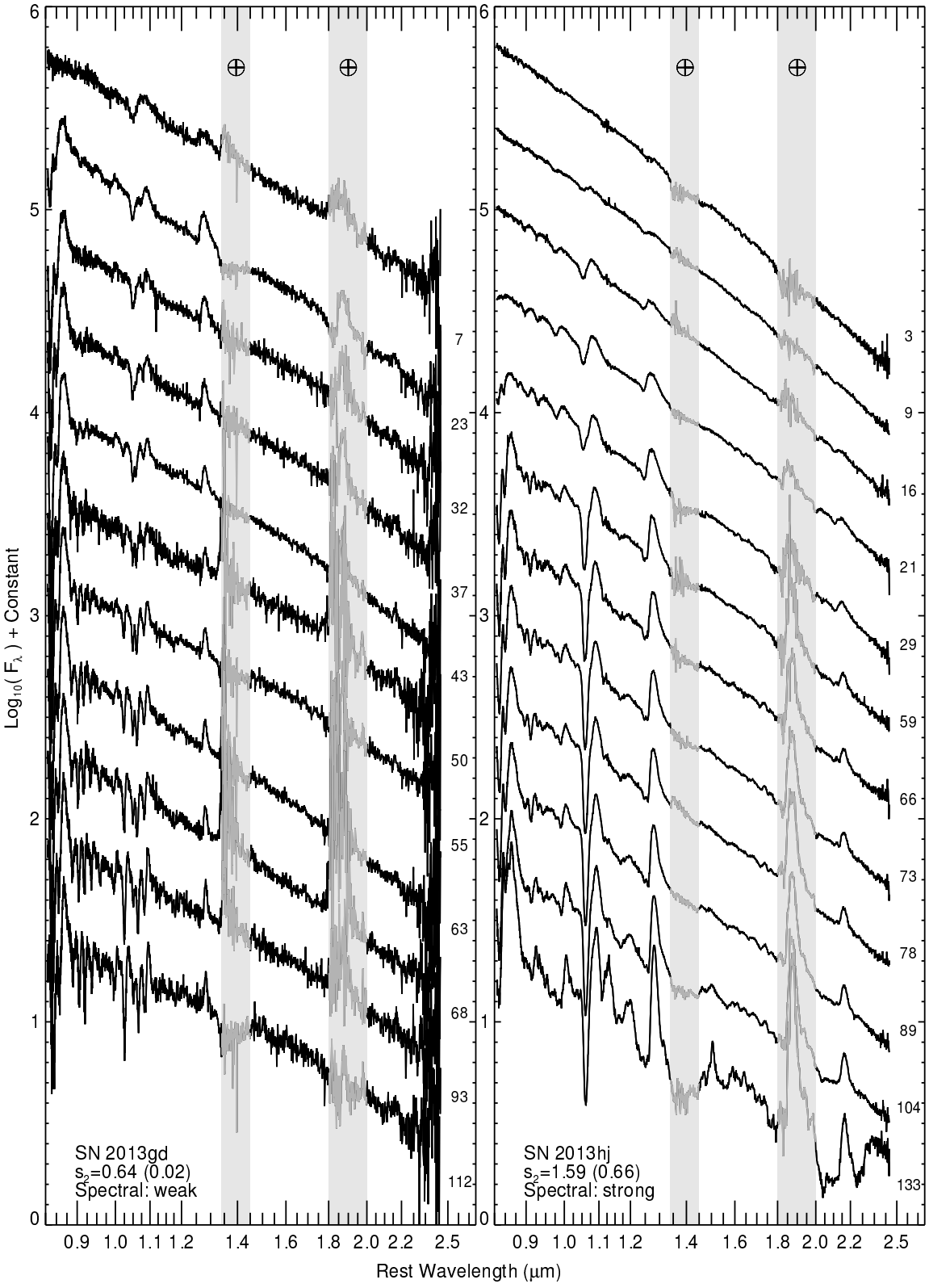

Figure 3. Same as Figure 2 but for SNe 2013hj and 2013gd, the two most complete time series in the sample.

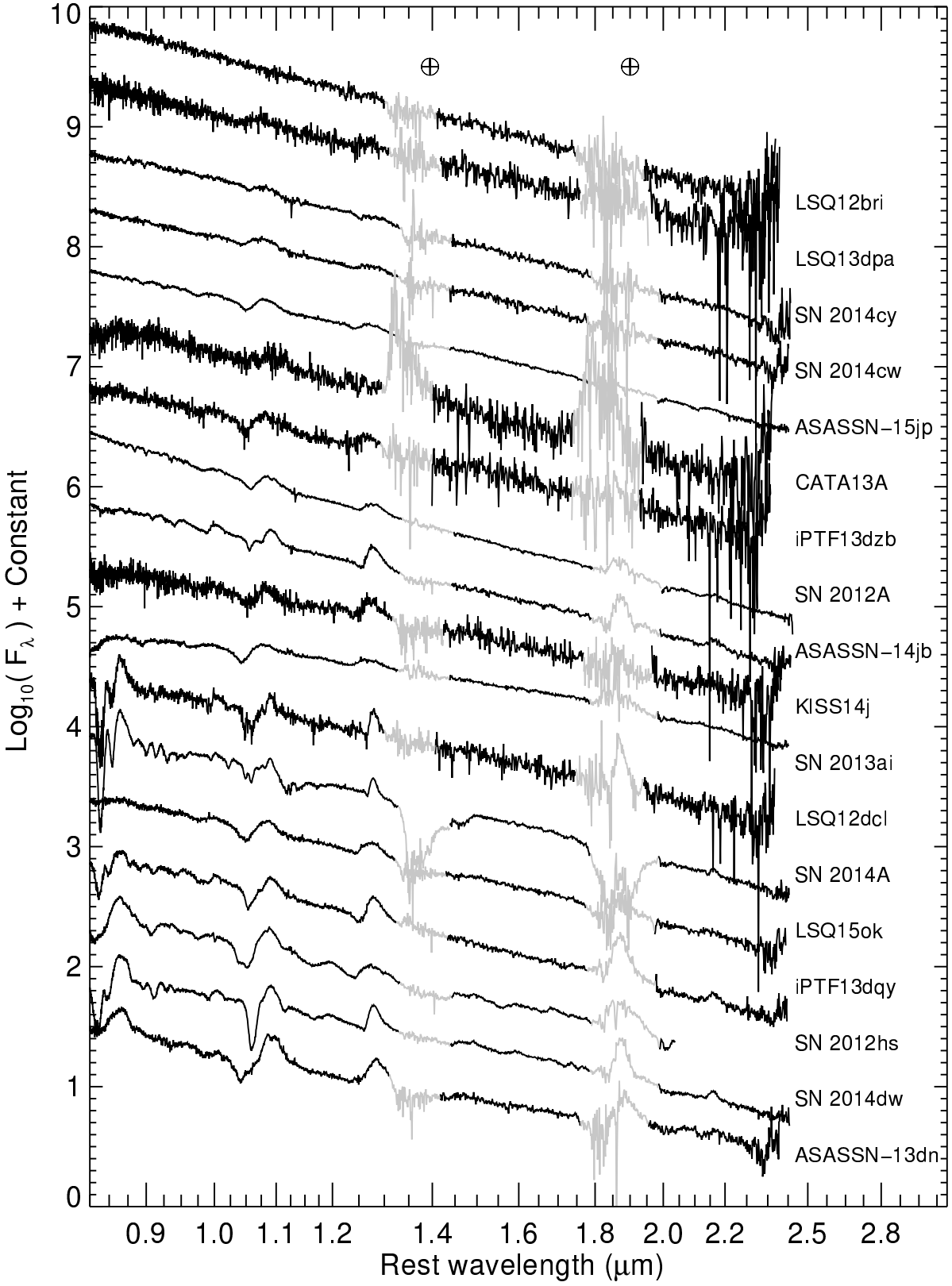

Figure 4. All SNe II with only one spectrum from the CSP-II sample. Wavelengths that have high telluric absorption are plotted in grey. Explosion date for most SNe are uncertain, and thus, the spectra are grouped by similarity of features present.

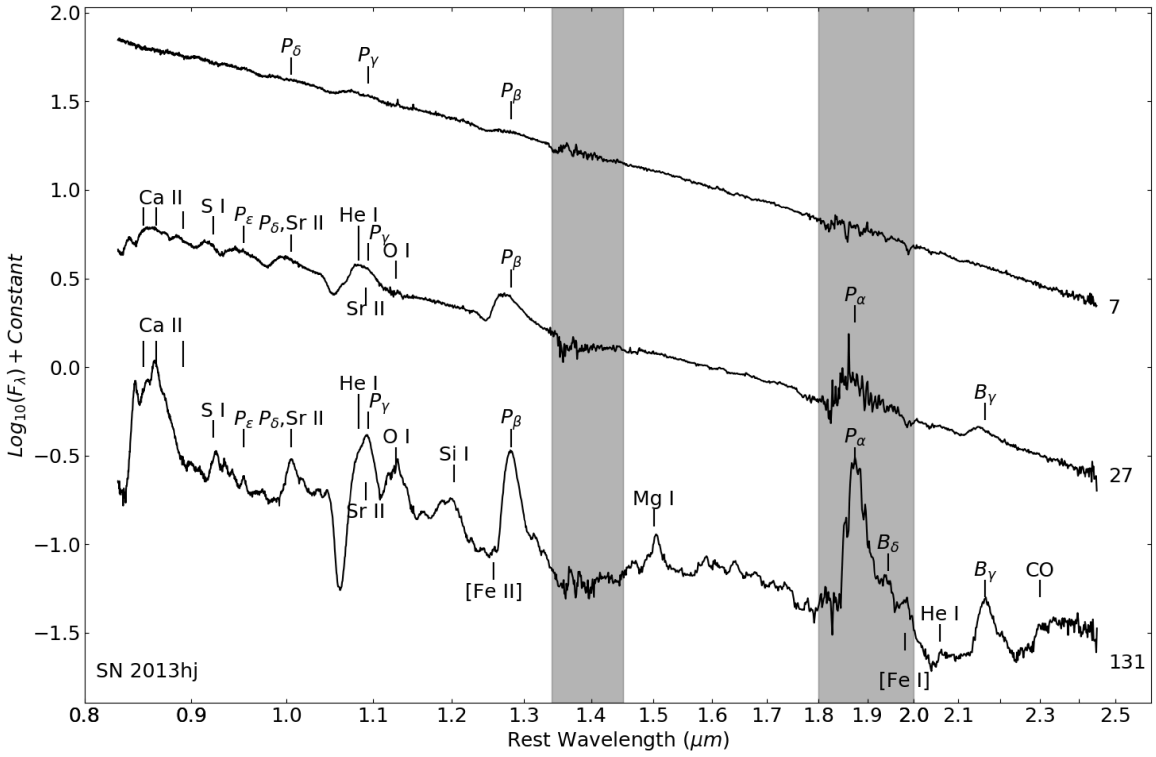

Figure 5. Time series spectra of SN 2013hj with the dominant ions labeled. The number to the right of each spectrum denotes the phase in days since explosion. The vertical lines mark the rest wavelength of each ion species. Regions of strong telluric absorption are outlined in grey.

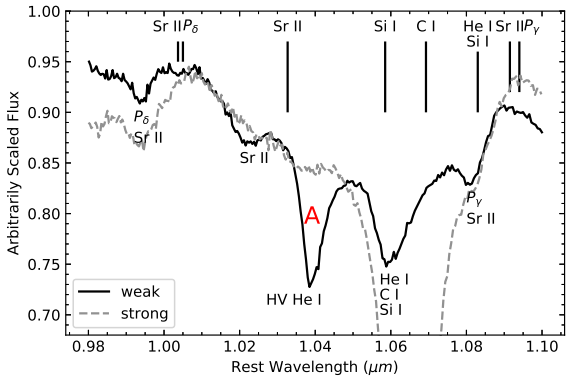

Figure 6. ∼30 day spectra of the *weak* SN 2012aw (black) and the *strong* SN 2013hj (grey) zoomed in on the region around He I $\lambda1.083\,\mu$m. The absorption and emission components of each line in the SN 2012aw spectrum are labeled with possible identifications. Emission features are marked at rest wavelength above the spectra. SN 2013hj is shown for comparison of line strengths and features present in the region. SN 2012aw and SN 2013hj are good representations of the weak and strong spectral classes, respectively. These features are discussed in detail in Section 6.

that exhibit a deeper He I. The P_γ/Sr II absorption appears earlier in these SNe and an additional absorption appears on the blue side of He I, hereafter feature A (Figure 6).

Feature A, if present, appears before the plateau and is similar to the He I $\lambda1.083\,\mu$m transition at these early times. During the plateau, feature A does not significantly increase in strength compared to the other absorption features in the spectrum and becomes less prominent compared to He I absorption in the same region.

O I $\lambda1.129\,\mu$m appears on the red side of the P_γ emission towards the end of the plateau phase. Si I $\lambda1.203\,\mu$m is also seen during this period and strengthens over time.

P_β $\lambda1.282\,\mu$m is seen at the beginning of the plateau and exhibits a symmetric P Cygni profile, that becomes dominated by its emission feature with very little absorption. Towards the end of the plateau, the P_β line profile seems to widen, likely due to the presence of a Si I multiplet in the region.

P_α $\lambda1.875\,\mu$m is seen early during the plateau, appearing predominately in emission. It may form earlier, along with the other Paschen series lines; however, it is located in a band of strong telluric absorption making it difficult to study for most spectra. Looking at SNe II with high signal-to-noise (S/N) ratios in this region, we see that P_α increases in strength over time. In the same band of telluric absorption, P_ϵ $\lambda0.954\,\mu$m and the Brackett series hydrogen line B_δ $\lambda1.944\,\mu$m appear around 30 days post explosion as weak emission features. These lines originate from the same upper level and thus both grow in strength with neither getting particularly strong compared to the other hydrogen emission features seen.

B_γ $\lambda2.165\,\mu$m shows up around the same time as P_α and cannot be resolved if the signal-to-noise ratio (S/N) of the spectrum is low, e.g., in some of the SN 2013gd spectra. The absorption of B_γ is weak enough that it can only be seen in the highest S/N spectra within the sample. The emission is also weak when compared to the Paschen-series.

4.3. *Radioactive Decay Tail*

After the plateau phase ends, we observe more metal lines forming, mostly in emission, and the emission component of all lines which formed during the plateau strengthen.

[Fe II] $\lambda1.279\,\mu$m, Mg I $\lambda1.503\,\mu$m and [Fe I] $\lambda1.980\,\mu$m emerge during the radioactive decay tail as weak emission features. Some SNe, e.g. SN 2013gd, do not show significant Mg I emission at any time. He I $\lambda2.058\,\mu$m appears as a weak absorption and does not appear in all SNe II. This He I $\lambda2.058\,\mu$m transition should be highly correlated with the He I $\lambda1.083\,\mu$m transition.

CO begins to appear after the plateau. The first CO overtone appears largely as emission features around $2.3\,\mu$m. The earliest detection in this data set is found in the SN 2013by spectrum taken 95 days post explosion. The CO feature becomes stronger over time, appearing in more SNe II around 120 days post explosion. We find CO in four SNe II within our sample, appearing in most spectrum taken after 120 days post explosion.

Late time spectra with possible CO detections are shown in Figure 7. Modeling and further analysis of CO will be performed in future work.

5. FEATURE MEASUREMENTS

The NIR spectral features were measured as outlined in Section 3.2 and are presented below. Figures 8 and 9 show the velocity and pEW evolution for the CSP-II sample over time, respectively. Figures 8 and 9 present the data split by s_2 in order to search for any relationships between photometric and NIR spectral properties.

He I $\lambda1.083\,\mu$m strengthens over time until nebular phases and often has the highest absorption pEW, increasing from 10 Å to $\sim 50-100$ Å, in the NIR spectrum. There is a dichotomy seen in the He I pEW, SNe well above 50 Å and those below 50 (Figure 9 top right panel). The velocity of He I absorption decreases over time, similar to the other spectral features, going from $\sim$ 11000 km s^{-1} at early times to $\sim$ 4000 km s^{-1} after the plateau phase ends.

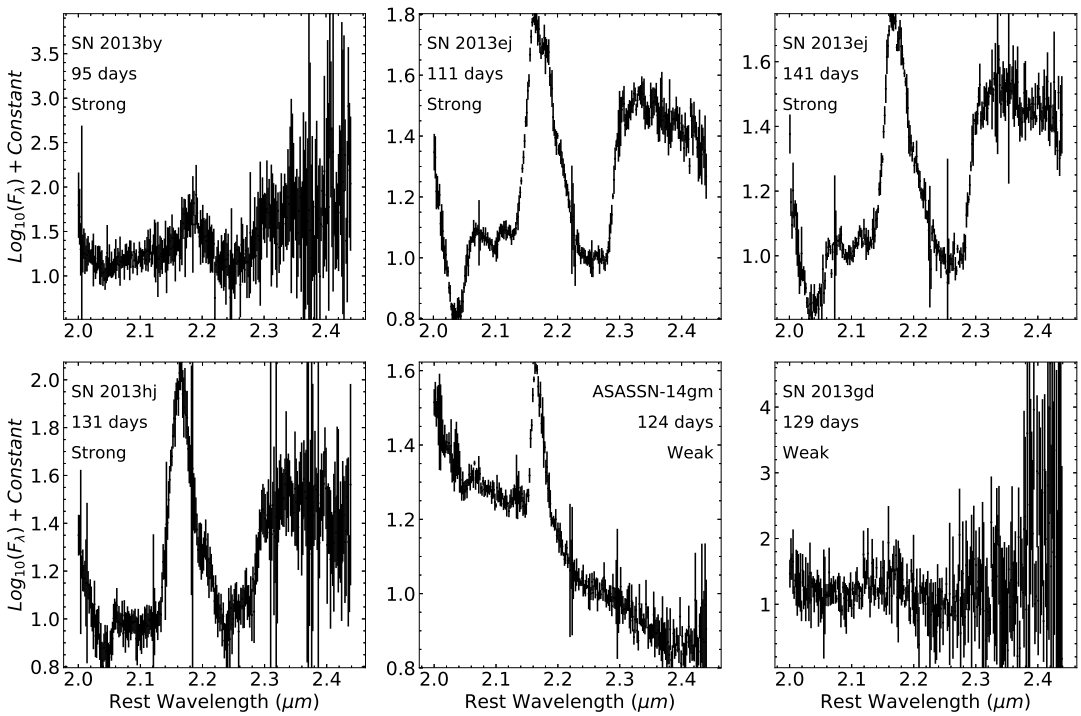

Figure 7. Late time spectra zoomed in on the region where CO is expected, around 2.35 μm. ASASSN14-gm and SN 2013gd have the weakest CO features (if present at all) past 120 days post explosion seen in the CSP-II sample.

The velocity of the P_β absorption at early and late times is nearly uniform among the sample, however, during the plateau there is a split in the velocities between fast and slow decliners, ∼7500 km s^{-1} for fast decliners and ∼4500 km s^{-1} for slow decliners. The absorption pEW increases from $\sim 1-2$ Å to 10 Å during the plateau. The emission pEW increases to over 100 Å during the plateau, becoming the second strongest emission, behind P_α, during this period. The emission velocities and absorption/emission pEWs show no correlation with photometric subclass.

The absorption and emission equivalent widths of the P_δ P Cygni profile do not increase as quickly as other hydrogen features. With velocities around 11000 km s^{-1}, P_δ often has the lowest velocities of all present hydrogen features, especially in fast declining SNe where the P_β velocities are higher, at certain epochs, than in slow declining SNe. The P_δ velocities are likely influenced by the Sr II λ1.092 μm blend causing them to be lower than expected. The P_δ absorption pEW evolves much like P_β going from $\sim 1-2$ Å to 10 Å during the plateau. The emission pEW is uniform amongst the sample, evolving linearly over time from $\sim 1-2$ Å to 50 Å at 120 days past explosion.

Feature A has the most inconsistent evolution, in velocity and pEW, compared to other NIR features (Figure 10). This feature has been previously identified as either Si I λ1.033 μm or high-velocity He I λ1.083 μm (Takáts et al. 2014). The absence of other metal lines in the spectra at similar times suggests that feature A is not Si I. Furthermore, the timing of the feature also suggests it is not Si as the photosphere is not expected to be in the metal rich region or the inner region of the hydrogen-rich envelope at these early epochs. Therefore, we conclude that feature A is most likely high-velocity He I. If present in a SN, it appears early, for example 7 days past explosion in SN 2013gd, and does not change significantly over time in pEW or velocity (Figure 11). The early onset of the feature suggests that it was produced in the outermost layer of the envelope. Unlike the photospheric He I absorption, feature A does not appear at the same wavelength in each SN, if it appears at all. It has a velocity spread between objects of ∼ 4000 km s^{-1} at similar epochs. This velocity spread assumes the feature is He I.

6. OBSERVED NIR DICHOTOMY

NIR spectra of SNe II are generally uniform showing the same features with similar time evolution between SNe. However, they exhibit a dichotomy of properties that emerges around 50 days post explosion and lasts until the end of the SN plateau phase. This is most prominent in the region around He I λ1.083 μm; a comparison between the two groups is shown schematically in Figure 6. Therefore, we classified our sample of SNe II

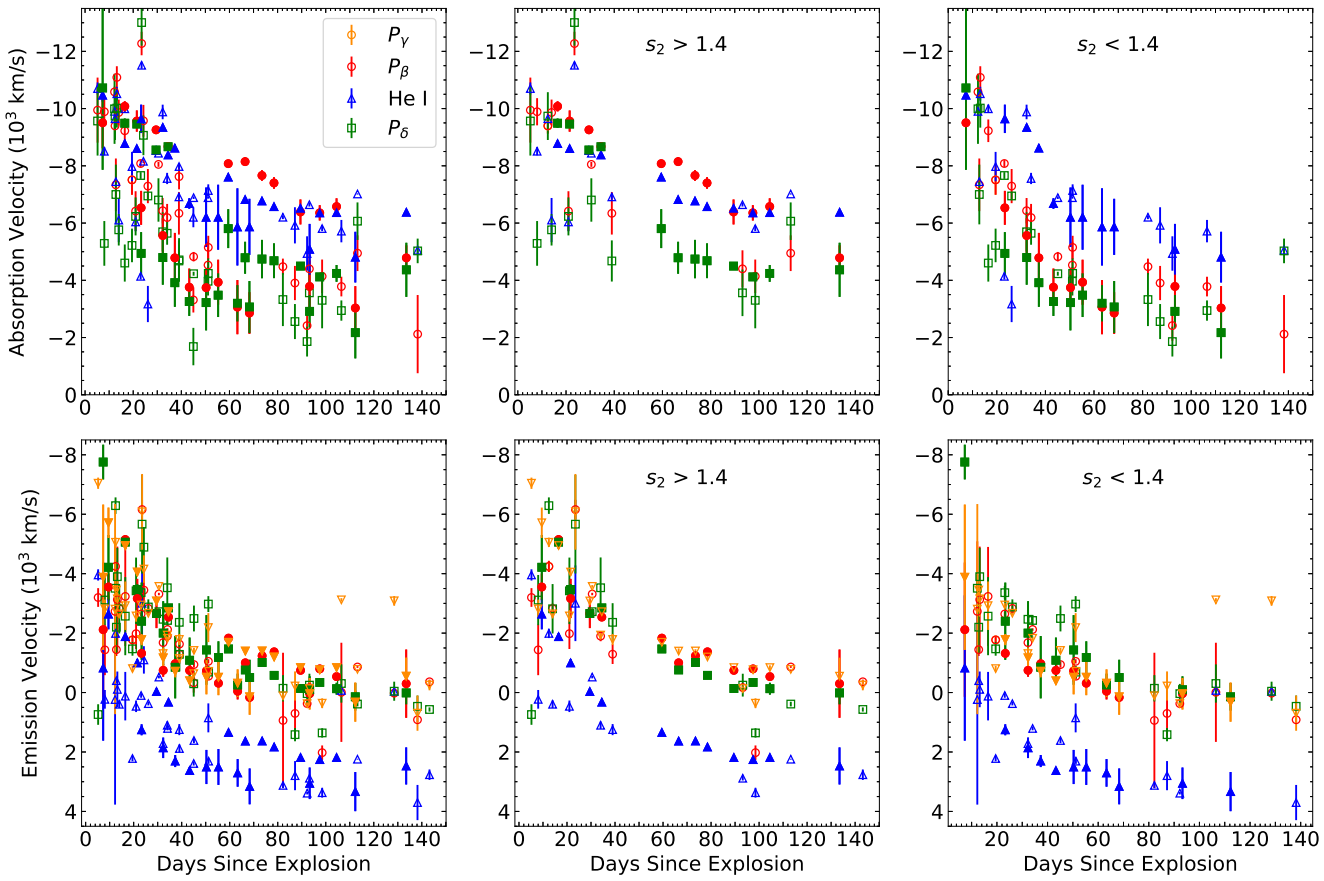

Figure 8. Evolution of the absorption and emission NIR velocitiy features of SNe II. The first column shows all of the CSP-II data together. The last two columns show the data split by s_2 value as defined in Section 3.1. Velocity measurements of He I $\lambda 1.083\,\mu$m are also included. The velocity evolution of the emission features is similar to what was seen by Anderson et al. (2014). The fast declining SN 2013hj and slow declining SN 2013gd are represented by filled points.

based on this dichotomy and describe the differences between the two groups (*weak* and *strong*) below.

We define *weak* SNe II as those with He I $\lambda 1.083\,\mu$m absorption pEW less than 50 Å after 50 days from explosion and *strong* SNe II with He I pEW greater than 50 Å. This quantitative division was arbitrarily chosen based on Figure 9. There are no SNe with intermediate pEW ($50 - 75$ Å) in our sample (histogram in the top right panel of Figure 9 shows the pEW of each SN interpolated to 75 days). Figure 11 shows all the SNe in the sample that could be classified as *weak* or *strong*. Although the pEW of He I was used to classify the two groups, several other differences between the two groups are also observed.

Weak SNe show an accompanying absorption feature, feature A, on the blue side of He I, and *strong* SNe do not. As discussed in Section 4.2, feature A is most likely high velocity He I $1.083\,\mu$m. Feature A always shows up before photospheric He I $1.083\,\mu$m, consistent with the interpretation that feature A is HV He I. *Weak* SNe show earlier notches arising from P_γ/Sr II absorption on the blue side of the He I/H I emission, ∼20 days past explosion. *Strong* SNe show the P_γ/Sr II absorption at ∼ 40 days. *Weak* SNe tend to exhibit strong Sr II features in the $1.0 - 1.1\,\mu$m region sooner, ∼ 20 days. *Strong* SNe may not show Sr II at all, e.g. SN 2013hj. *Weak* SNe have a more layered velocity structure and decline in velocity more quickly than *strong* SNe (Figure 8). CO emission can be seen in *strong* SNe before 100 days past explosion. Emission from the first CO overtone appears at later times, past 120 days, in *weak* SNe, if seen at all.

In the optical, a small notch on the blue of the H_α absorption was interpreted as HV H I, after 30 days post explosion, and its evolution is well-studied (Gutiérrez et al. 2017a). Following Takáts et al. (2014), we compare the evolution of these HV features in Figure 12 to determine if the features are formed in the same region. In our sample only one SN II shows both HV features: SN 2012aw. However, this does not mean that the HV H I is absent in all other SNe II, as it could be mixed

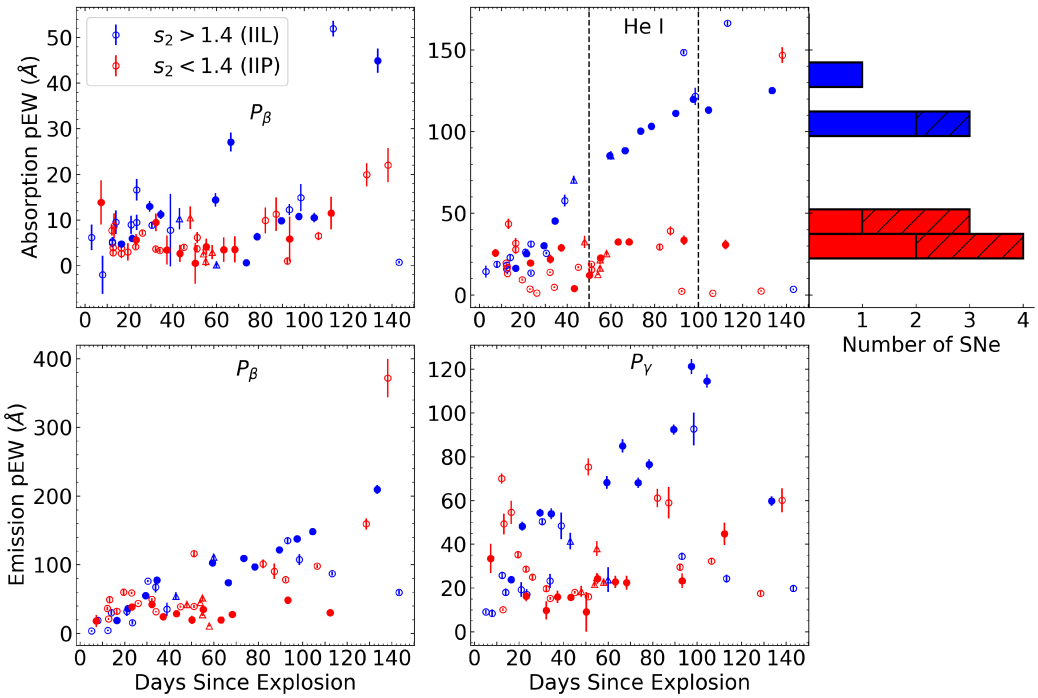

Figure 9. Evolution of the absorption and emission pEW width of SNe II NIR features over time. Included are pEW measurements of He I $\lambda 1.083\,\mu$m. There is a stark contrast between slow and fast declining SNe II with regards to He I absorption pEW. The emission pEW also splits with ASASSN-15bb being the sole slow declining SN II lying with the fast declining SNe II curve. The fast declining SN 2013hj and slow declining SN 2013gd are represented by filled circles. SNe not from CSP-II are plotted as open triangles. The vertical black lines drawn in the upper right panel represent the time in which a SN II with $s_2 = 1.4$ should be in its plateau phase, when a NIR classification can be made. The histograms show how many SNe lie between 50 and 100 days past explosion. SNe not from CSP-II are plotted with hatched patterns in the histograms. The histogram shows all data between $50 - 100$ days interpolated to 75 days.

into H_α as suggested by Chugai et al. (2007). H I is also easier to excite than He I, which could explain the higher incidence of HV H I in the optical. It is possible for a SN to show a feature which looks similar to HV H I and no NIR HV counterpart, e.g. SN 2013ej. The absorption on the blue side of H_α in the optical may also be due to Si II as suggested by Valenti et al. (2014) for SN 2013ej. When these HV components appear in the same SNe, their velocities match, e.g. SN 2012aw with HV H I and HV He I both around 14000 km s^{-1}.

The NIR spectroscopic classification of *weak* and *strong* are found to have a one-to-one correspondence with the IIP and IIL subclasses, based on the decline rate s_2. For the SNe in our sample where we can determine a photometric classification (5 slow decliners and 4 fast decliners), all slow decliners are *weak* and all fast decliners are *strong*. When we include all of the previously published data that can be spectroscopically classified, either by pEW measurements or by the line profiles in the region around He I $\lambda 1.083\,\mu$m (8 slow decliners and 2 fast decliners), we find only one exception to the rule, SN 2012A (Tomasella et al. 2013). Looking at NIR spectra, the strong dichotomy suggests that fast declining and slow declining SNe II are two distinct groups of objects, at least phenomenologically; whereas when viewed in the optical, these objects appear to have a continuous range of photometric and spectroscopic properties (Anderson et al. 2014; Gutiérrez et al. 2017a,b; Pessi et al. 2019). A Silverman model (Silverman 1981) was used to create s_2 probability density functions (PDF) for both the CSP-II and Gutiérrez et al. (2017b) photometric samples. A Silverman model assumes that each point can be represented by a Gaussian profile. These profiles can then be added together and normalized to create a PDF of the dataset. A PDF was made using the error from each s_2 measurement, however, for the majority of measurements this error is small compared to the s_2 value and produces a PDF that over-estimates the number of measurement modes. Thus, each point in the Silverman model is assigned the same kernel density that was chosen using the critical width function of Silverman (1981). The resulting PDFs of the two samples are similar despite the small num-

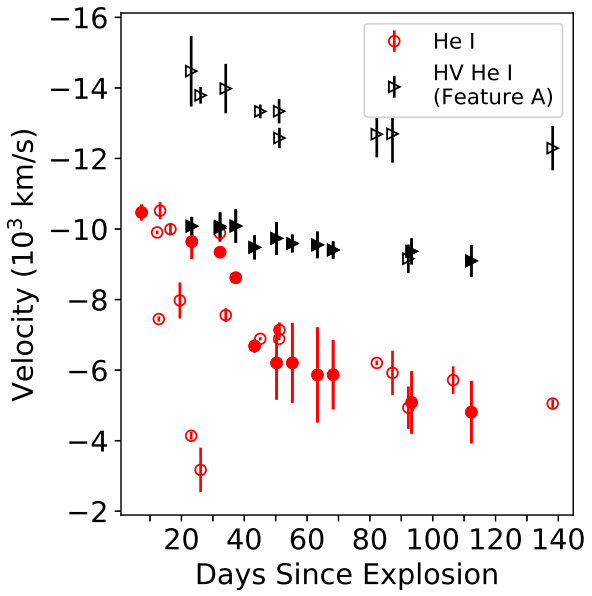

Figure 10. Velocity comparison of feature A and the He I $\lambda 1.083\,\mu$m absorption for each SN in which both profiles are present. These velocities assume the rest wavelength of He I $\lambda 1.083\,\mu$m. SN 2013gd is represented by filled points. Feature A exhibits a flat velocity evolution, unlike any other feature in a SN II spectrum. Feature A also has a large velocity spread, as low as 10000 km s^{-1} and as high as 14000 km s^{-1}. Feature A is most likely HV He I.

bers of the CSP-II sample, suggesting that the CSP-II sample is not photometrically biased.

7. PRINCIPLE COMPONENT ANALYSIS

To further test the validity of the dichotomy observed in the NIR spectra of SNe II, we performed a principal component analysis (PCA) on a selection of data within our sample. PCA has been applied in a variety of astronomical research previously (e.g. Suzuki 2006; Hsiao et al. 2007) to recognize patterns in the data and as a tool for creating spectral templates. PCA reduces the dimensionality of a multi-dimensional data set, such that a large fraction of the variance in the data is captured in a few principal components.

We require that each input spectrum for PCA have a S/N of at least 50 in the telluric regions, $1.35-1.45\,\mu$m and $1.80-2.00\,\mu$m, as PCA is susceptible to noise spikes. The zeroth principal component makes up ∼50% of the total variance of the spectrum, as shown in Figure 13. This component describes the slope, line strength, and velocity over time of the SNe II, suggesting these spectral properties are all correlated. There is a strong correlation between the projections of observed spectra onto the zeroth principle component and phase, as expected, since the line strengths of most features increase with time. The first component picks out ∼ 31% of the variance and shows further color and calcium changes when the region around He I $\lambda 1.083\,\mu$m is uniform. The second component makes up ∼ 6% of the total variance and is of particular interest as it picks out the difference in this region between *weak* and *strong* SNe II. The dichotomy of the region around He I $\lambda 1.083\,\mu$m motivated splitting the sample into two templates and further supports the two distinct groups outlined in Section 6.

Cosmological studies using both Type II and Type Ia SNe are pushing into the NIR to minimize the effect of dust extinction (e.g. Rodríguez et al. 2019), and representative spectral templates of all types of SNe are crucial for future SN cosmological experiments. The two spectral templates are split by classification of *weak* and *strong* He I $\lambda 1.083\,\mu$m absorption and are created by polynomial fitting to the projections over time. The resulting *strong* and *weak* templates are plotted, with different colors representing differents epochs, in Figure 14. We conclude that slow declining SNe II (conventionally IIP) are best represented by the *weak* spectral template while the *strong* template better fits fast declining SNe II (conventionally IIL). Our template spectra can be found on the Web.[3]

8. DISCUSSION

Due to the homogeneity of the hydrogen rich envelope, the difference in spectral features between fast and slow declining SNe II most likely comes from explosion energy and temperature changes (Hoeflich 1988; Takeda 1990; Duschinger et al. 1995; Gerardy et al. 2000). The light curves are powered by the energy stored by the hydrodynamical shell during the early phase, the heating by radioactive decay of $^{56}Co \rightarrow^{56} Ni \rightarrow^{56} Fe$, and the recombination energy. During the plateau phase, the opacity drops by several orders of magnitude from the outer recombined layers above the photosphere to the inner ionized layers. The release of stored energy and the recombination of hydrogen powers the plateau phase (Chieffi et al. 2003). The luminosity drops when the recombination front reaches the inner edge of the hydrogen-rich layers. The total energy released and the duration of the plateau decreases with the total hydrogen mass and, eventually, marks the transition from slow declining SNe II with long plateaus to fast declining SN II; however, explosion energy likely plays a significant role (Popov 1993). With increasing hydrogen-mass, the C/O-rich layers are exposed later. This may explain why in SNe II *weak* we see later emission from the first

[3] https://csp.obs.carnegiescience.edu/data

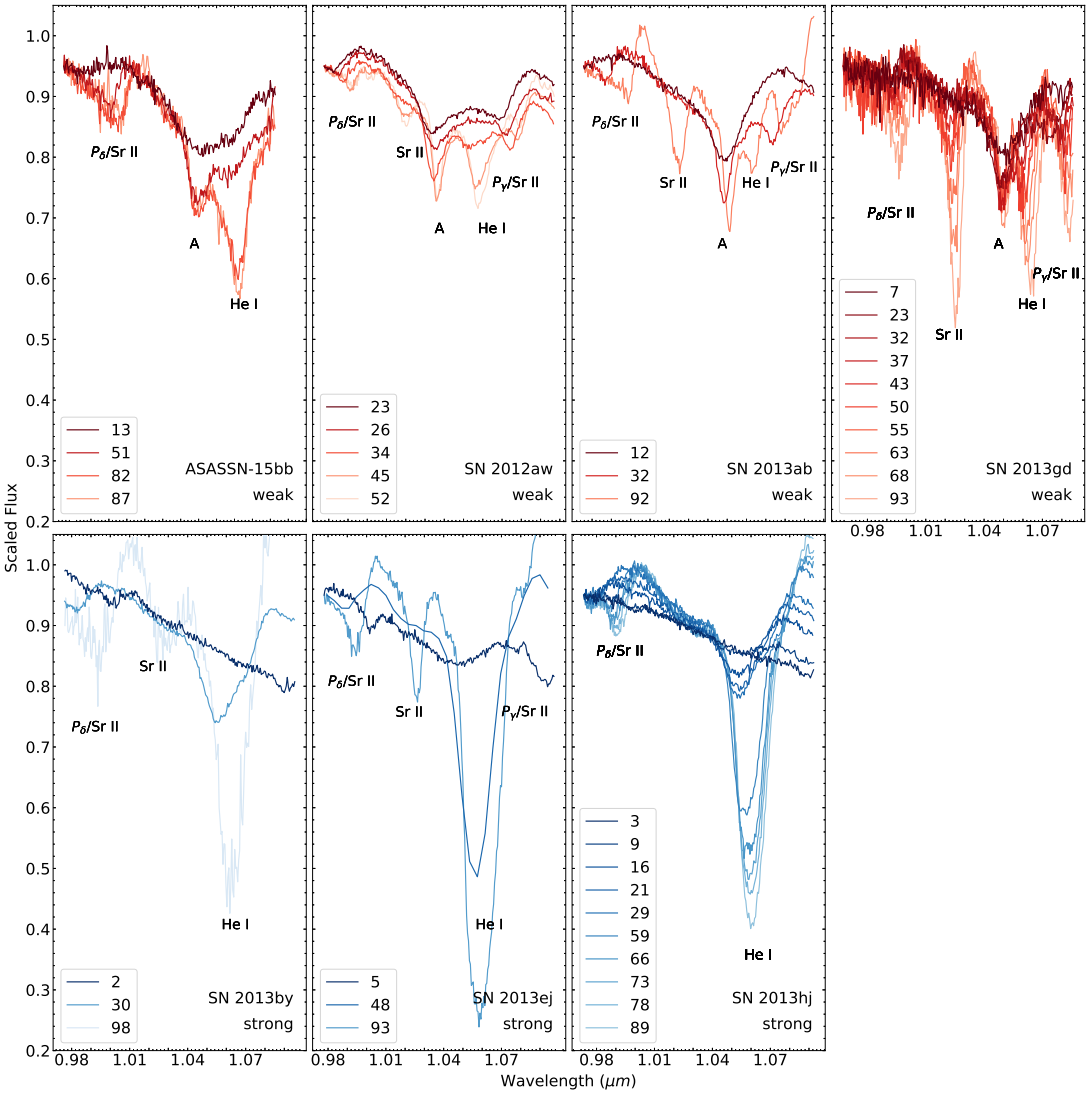

Figure 11. All SNe from the CSP-II sample that could be classified as either *strong* or *weak*. *Weak* SNe are plotted in red and *strong* SNe are plotted in blue. Ion names mark the most likely dominant species for each absorption feature. The *weak* SNe exhibit a range of strength and velocity evolutions within the subclass, however, can still be defined by weak He I absorption and the presence of feature A. Feature A is most likely HV He I.

overtone of the CO band (Gerardy et al. 2000; Smith et al. 2001; Matsuura 2017; Banerjee et al. 2018), pointing to a mass sequence.

Progenitors of slow declining SNe II have been interpreted to have lower zero-age main sequence mass than those of fast declining SNe II, as they have retained much of their hydrogen envelope (Heger et al. 2000). Alternatively, Morozova et al. (2017, 2018) suggest that SNe IIL may be the result of a RSG surrounded by dense circumstellar material. If SNe IIL have lost some of their hydrogen envelope, the process in which they lose this mass is uncertain. We cannot make a distinction in this work between SNe which have lost some of their hydrogen envelope by wind or a common envelope phase.

The longer lifetime of presumably lower mass progenitors of the slower declining SNe II leading up to the explosion allows more s-process elements, such as Sr, to be produced, providing a possible explanation for the Sr II lines observed mostly in the SNe II *weak* class (Limongi et al. 2000). However, we see no correlation with spectral type and progenitor mass, determined using pre-explosion images, for those SNe within our sample and the sample of Smartt (2015), possibly due to the large uncertainty in mass.

The mixing of ^{56}Ni to high velocities could explain the pEW difference between SNe II *weak* and *strong*. The presence of He I requires high energy non-thermal photons close to the He layer Graham (1988). This can

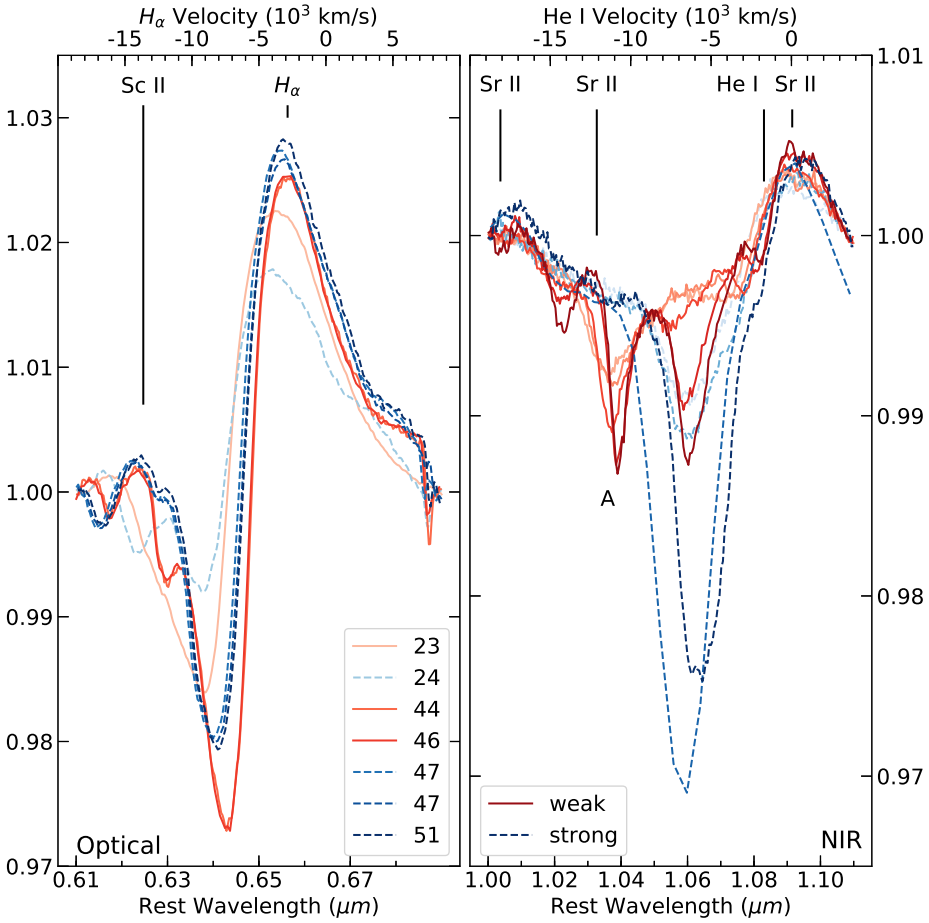

Figure 12. Comparison of the optical (left) and NIR (right) data of the two spectral classes. The *weak* spectral class is plotted in red with darker shades representing later phases. The *strong* spectral class is plotted in blue with darker shades representing later phases. The phase of each spectrum, rounded to the nearest day, is listed in the left panel. Both spectral types are plotted at similar phases. In the optical SN 2013ej (*strong*) and SN 2012aw (*weak*) are plotted. In the NIR SN 2013hj (*strong*) and SN 2012aw (*weak*) are plotted. SN 2013hj has little optical data but is spectroscopically similar to SN 2013ej in the NIR so we use SN 2013ej as the *strong* spectral class representation in the optical. The difference between these two classes is much more obvious in the NIR.

only be achieved by gamma rays produced from the radioactive decay of ^{56}Ni.

Multiple scenarios exist to explain the HV features in the spectral *weak* class. The most likely explanation is from thermal excitation produced by a reverse shock as a result of the interaction between the SN ejecta and wind (Chugai et al. 2007), in which H and He are excited by X-rays, with the HV H possibly mixed into H_α and HV He present in the NIR. Alternatively, Dessart, & Hillier (2008) suggest a radiation transport effect in layers with certain density slopes where hot, high-density inner layers and low-density outer layers with long recombination times are separated by a region of low excitation common to all SNe II. However, this theory does not explain why these *weak* features are not seen in fast declining SNe II. Moreover, the models of Dessart, & Hillier (2008) predict He I showing up first and vanishing after $\sim$ 20 days, in contradiction to the observations. Thus we believe the HV features seen are powered by a shock.

9. CONCLUSIONS

We have presented 81 NIR spectra of 30 SNe II observed between 2011 and 2015 as part of the CSP-II. The spectra range between 1 and 150 days post explosion. Using V-band light curves, photometric properties were measured for 14 SNe within the sample. The evolution of NIR spectral features was outlined and for the most dominant features, pEW and velocities were systematically measured.

There is a strong dichotomy in the NIR spectral features of SNe II, and it is the most prominent in the

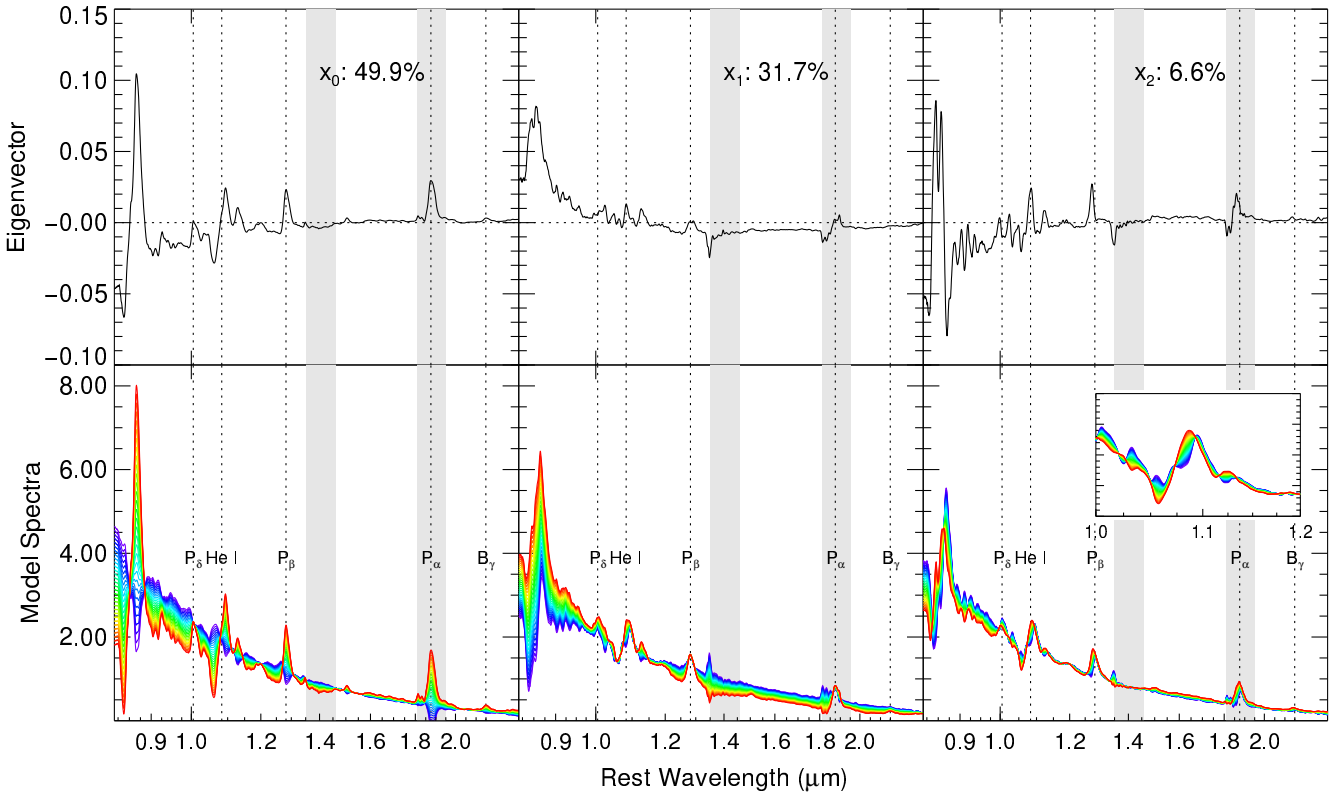

Figure 13. Principal component model of the SNe II spectrum. The first three components are shown with the effects of 3σ variation. The eigenvalue for each projected component is noted on top as a percentage of the total variance. Rest wavelengths of the strongest features are plotted as vertical dashed lines: P_α, P_β, He I, and P_δ. The zeroth component represents the color and strength of features making up the spectrum over time. The first component shows calcium changes that vary with SN color. The second component picks out the different spectral classes, *weak* and *strong*. The bottom left panel also shows the zoomed in region from $1.0 - 1.2\,\mu$m where the spectral dichotomy is seen. The colors show deviations from the mean spectrum of $\pm 3\sigma$.

features around He I $\lambda 1.083\,\mu$m. Thus, we presented spectral classifications based on the strength of this feature: *strong* and *weak* SNe II. Characteristics of the two classes are outlined as follows:

- *Weak* SNe show an accompanying absorption feature on the blue side of the He I $\lambda 1.083\,\mu$m, feature A, which we interpret as a HV component of the same He I line, and *strong* SNe do not. The HV He I line always has an earlier onset then the photospheric He I $\lambda 1.083\,\mu$m absorption feature.

- *Weak* SNe show earlier absorption, ~ 20 days past explosion, from P_γ/Sr II than *strong* SNe. *Strong* SNe show this feature at ~ 40 days.

- *Weak* SNe more often exhibit Sr II features in the $1.0 - 1.1\,\mu$m region.

- *Strong* SNe can form the first overtone of CO at earlier times, less than 100 days. *Weak* SNe have later formation of CO, past 120 days.

We found that these spectral classifications of *strong* and *weak* SNe correspond to the plateau decline rate: slow declining SNe II (IIP) are *weak* and fast declining SNe II (IIL) are *strong*. This a somewhat surprising result given the previous research showing a continuum in optical light curves and spectroscopic features. The HV He I feature seen is most likely due to a reverse shock as explained in Chugai et al. (2007). However, this does not explain the dichotomy. PCA was performed on the spectra which further confirmed the observed dichotomy that represented $\sim$ 6% of the spectroscopic variance. Finally, using PCA, two spectral templates for SNe II were created, SNe *weak* and *strong*. These templates are crucial for cosmological studies using SNe II.

The authors would like to thank the anonymous referee for their comments. The work of the CSP-II has been generously supported by the National Science Foundation (NSF) under grants AST-1008343, AST-1613426, AST-1613455, and AST-1613472. The CSP-II

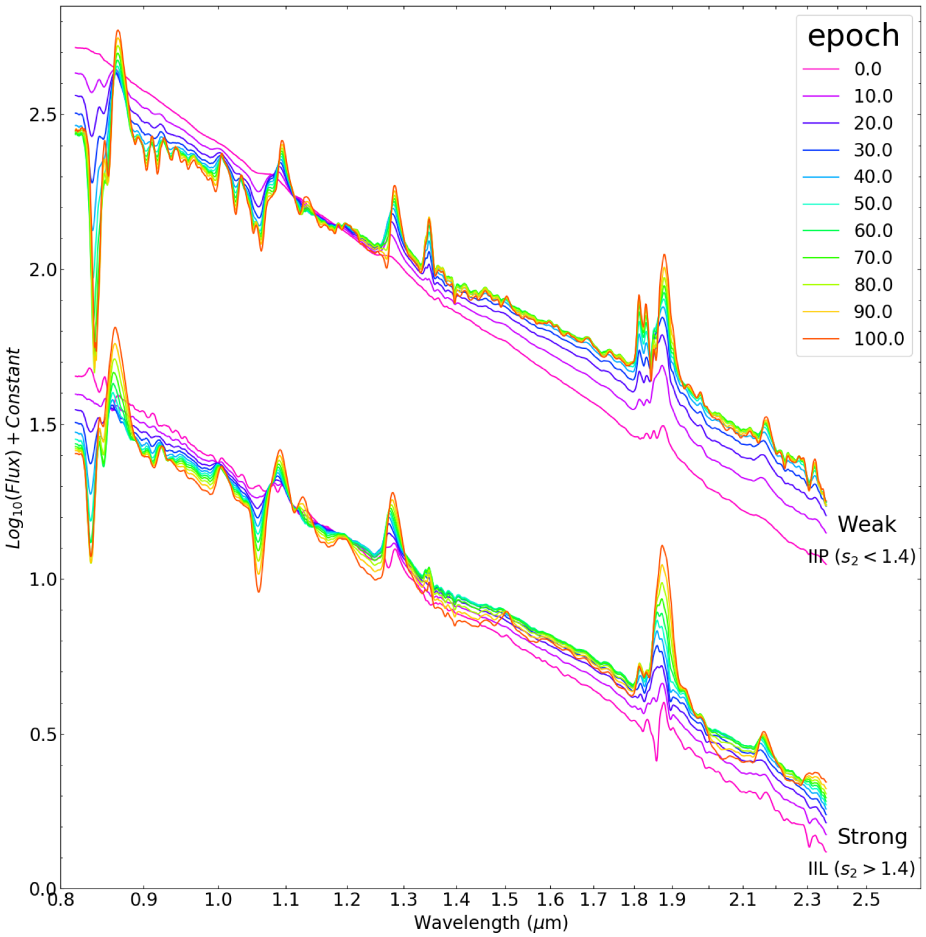

Figure 14. Time evolution of the two spectral templates; *weak* and *strong* SNe II corresponding to slow and fast declining SNe II (IIP and IIL, respectively). Different epochs are shown in color to illustrate the evolution over time of the models.

was also supported in part by the Danish Agency for Science and Technology and Innovation through a Sapere Aude Level 2 grant.

We would like to thank Michael Cushing for his work on Spextool in processing low-resolution data. PH acknowledges support by the NSF grant 1715133. Research by DJS is supported by NSF grants AST-1821987, AST-1821967, AST-1813708, and AST-1813466. CPG acknowledges support from EU/FP7-ERC grant no. [615929]. Support for JLP is provided in part by FONDECYT through the grant 1191038 and by the Ministry of Economy, Development, and Tourisms Millennium Science Initiative through grant IC120009, awarded to The Millennium Institute of Astrophysics, MAS.

Software: firehose (Simcoe et al. 2013), xtellcor (Vacca et al. 2003), Spextool (Cushing et al. 2004), SNID (Blondin, & Tonry 2007)

REFERENCES

Anderson, J. P., González-Gaitán, S., Hamuy, M., et al. 2014, ApJ, 786, 67.

Anderson, J. P., Dessart, L., Gutierrez, C. P., et al. 2014, MNRAS, 441, 671

Andrews, J. E., Sand, D. J., Valenti, S., et al. 2019, arXiv:1907.01013

Antezana, R., Hamuy, M., Gonzalez, L., et al. 2013, Central Bureau Electronic Telegrams 3757, 1.

Arcavi, I., Gal-Yam, A., Cenko, S. B., et al. 2012, ApJ, 756, L30.

Arnett, W. D. 1982, NATO Advanced Science Institutes (ASI) Series C, 221.

Arnett, W. D., Bahcall, J. N., Kirshner, R. P., & Woosley, S. E. 1989, ARA&A, 27, 629

Banerjee, D. P. K., Joshi, V., Evans, A., et al. 2018, MNRAS, 481, 806.

Barbon, R., Ciatti, F., & Rosino, L. 1979, A&A, 72, 287.

Baron, E., Nugent, P. E., Branch, D., et al. 2004, ApJ, 616, L91.

Benetti, S., Turatto, M., Balberg, S., et al. 2001, MNRAS, 322, 361.

Blondin, S., & Tonry, J. L. 2007, ApJ, 666, 1024.

Bose, S., Kumar, B., Misra, K., et al. 2016, MNRAS, 455, 2712.

Bostroem, K. A., Valenti, S., Horesh, A., et al. 2019, MNRAS, 485, 5120.

Bouchet, P., Stanga, R., Moneti, A., et al. 1987, European Southern Observatory Conference and Workshop Proceedings, 159.

Bouchet, P., Phillips, M. M., Suntzeff, N. B., et al. 1991, A&A, 245, 490.

Branch, D. 1987, ApJ, 320, L121.

Brimacombe, J., Kiyota, S., Holoien, T. W.-S., et al. 2014, The Astronomer's Telegram, 6592, 1.

Brimacombe, J., Holoien, T. W.-S., Stanek, K. Z., et al. 2015, The Astronomer's Telegram, 7320, 1.

Catchpole, R. M., Whitelock, P. A., Feast, M. W., et al. 1988, MNRAS, 231, 75P.

Catchpole, R. M., Whitelock, P. A., Menzies, J. W., et al. 1989, MNRAS, 237, 55P.

Chieffi, A., Domínguez, I., Höflich, P., et al. 2003, MNRAS, 345, 111.

Chugai, N. N., Chevalier, R. A., & Utrobin, V. P. 2007, ApJ, 662, 1136.

Cifuentes, M., Pignata, G., Apostolovski, Y., et al. 2012, Central Bureau Electronic Telegrams 3347, 1.

Conseil, E., Klotz, A., Coward, D., et al. 2013, The Astronomer's Telegram, 4849, 1.

Cushing, M. C., Vacca, W. D., & Rayner, J. T. 2004, PASP, 116, 362

Dall'Ora, M., Botticella, M. T., Pumo, M. L., et al. 2014, ApJ, 787, 139.

Danziger, I. J., Lucy, L. B., Bouchet, P., et al. 1991, Supernovae, 69.

Dessart, L., & Hillier, D. J. 2008, MNRAS, 383, 57.

Duschinger, M., Puls, J., Branch, D., Hoeflich, P., & Gabler, A. 1995, A&A, 297, 802

Elias, J. H., Gregory, B., Phillips, M. M., et al. 1988, ApJ, 331, L9.

Elmhamdi, A., Danziger, I. J., Chugai, N., et al. 2003, MNRAS, 338, 939.

Faran, T., Poznanski, D., Filippenko, A. V., et al. 2014, MNRAS, 445, 554.

Faran, T., Nakar, E., & Poznanski, D. 2018, MNRAS, 473, 513.

Filippenko, A. V., Matheson, T., & Ho, L. C. 1993, ApJL, 415, L103 .

Folatelli, G. 2004, NewAR, 48, 623

Fraser, M., Ergon, M., Eldridge, J. J., et al. 2011, MNRAS, 417, 1417.

Freedman, W. L., Madore, B. F., Gibson, B. K., et al. 2001, ApJ, 553, 47.

Galbany, L., Hamuy, M., Phillips, M. M., et al. 2016, VizieR Online Data Catalog , J/AJ/151/33.

Garavini, G., Folatelli, G., Nobili, S., et al. 2007, A&A, 470, 411.

Gerardy, C. L., Fesen, R. A., Höflich, P., et al. 2000, AJ, 119, 2968.

Gilliland, R. L., Nugent, P. E., & Phillips, M. M. 1999, ApJ, 521, 30.

Graham, J. R. 1988, ApJL, 335, L53

Gutiérrez, C. P., Anderson, J. P., Hamuy, M., et al. 2014, ApJ, 786, L15.

Gutiérrez, C. P., Anderson, J. P., Hamuy, M., et al. 2017, ApJ, 850, 89.

Gutiérrez, C. P., Anderson, J. P., Hamuy, M., et al. 2017, ApJ, 850, 90.

Hadjiyska, E., Rabinowitz, D., Baltay, C., et al. 2012, The Astronomer's Telegram, 4223, 1.

Hamuy, M., Pinto, P. A., Maza, J., et al. 2001, ApJ, 558, 615.

Hamuy, M., Folatelli, G., Morrell, N. I., et al. 2006, PASP, 118, 2.

Heger, A., Woosley, S. E., & Langer, N. 2000, NewAR, 44, 297.

Hoeflich, P. 1988, Proceedings of the Astronomical Society of Australia, 7, 434

Holoien, T. W.-S., Prieto, J. L., Kochanek, C. S., et al. 2014, The Astronomer's Telegram, 6436, 1.

Holoien, T. W.-S., Bersier, D., Stanek, K. Z., et al. 2015, The Astronomer's Telegram, 7546, 1.

Howerton, S., Drake, A. J., Djorgovski, S. G., et al. 2014, Central Bureau Electronic Telegrams 3773, 1.

Hsiao, E. Y., Conley, A., Howell, D. A., et al. 2007, ApJ, 663, 1187.

Hsiao, E. Y., Marion, G. H., Kirshner, R. P., et al. 2013, The Astronomer's Telegram, 5678, 1.

Hsiao, E. Y., Phillips, M. M., Marion, G. H., et al. 2019, PASP, 131, 14002.

Isaak, K. G., Priddey, R. S., McMahon, R. G., et al. 2002, MNRAS, 329, 149.

Jang, I. S., & Lee, M. G. 2014, ApJ, 792, 52.
Jerkstrand, A., Smartt, S. J., Fraser, M., et al. 2014, MNRAS, 439, 3694.
Kim, M., Zheng, W., Li, W., et al. 2013, Central Bureau Electronic Telegrams 3606, 1.
Kiyota, S., Holoien, T. W.-S., Stanek, K. Z., et al. 2015, The Astronomer's Telegram, 6936, 1.
Limongi, M., Straniero, O., & Chieffi, A. 2000, ApJS, 129, 625.
Luppi, F., Yusa, T., Koff, R. A., et al. 2012, Central Bureau Electronic Telegrams 2974, 2.
Lyman, J., Bersier, D., Dennefeld, M., et al. 2013, The Astronomer's Telegram, 5650, 1.
Maguire, K., Di Carlo, E., Smartt, S. J., et al. 2010, MNRAS, 404, 981.
Makarov, D., Prugniel, P., Terekhova, N., et al. 2014, A&A, 570, A13.
Mathewson, D. S., Ford, V. L., & Buchhorn, M. 1992, ApJS, 81, 413.
Matsuura, M. 2017, Handbook of Supernovae, 2125.
Maund, J. R., Smartt, S. J., & Danziger, I. J. 2005, MNRAS, 364, L33.
Maza, J., Gonzalez, S., Maureira, E., et al. 2013, Central Bureau Electronic Telegrams 3752, 1.
Meikle, W. P. S., Allen, D. A., Spyromilio, J., et al. 1989, MNRAS, 238, 193.
Meikle, W. P. S., Allen, D. A., Spyromilio, J., et al. 1991, Supernovae, 102.
Meikle, W. P. S., Spyromilio, J., Allen, D. A., et al. 1993, MNRAS, 261, 535.
Minkowski, R. 1941, PASP, 53, 224.
Mitra, A., Baumont, S., Le Guillou, L., et al. 2015, The Astronomer's Telegram, 7140, 1.
Moore, B., Newton, J., & Puckett, T. 2012, Central Bureau Electronic Telegrams 2974, 1.
Moriya, T. J., Pruzhinskaya, M. V., Ergon, M., et al. 2016, MNRAS, 455, 423.
Morokuma, T., Tominaga, N., Tanaka, M., et al. 2014, PASJ, 66, 114.
Morozova, V., Piro, A. L., & Valenti, S. 2017, ApJ, 838, 28
Morozova, V., Piro, A. L., & Valenti, S. 2018, ApJ, 858, 15
Nakano, S., Noguchi, T., Masi, G., et al. 2013, Central Bureau Electronic Telegrams 3671, 1.
Nishimura, K. 2014, Central Bureau Electronic Telegrams 3964, 1.
Oliva, E., Moorwood, A. F. M., & Danziger, I. J. 1987, International Astronomical Union Circular 4484, 1.
Olivares E., F., Hamuy, M., Pignata, G., et al. 2010, ApJ, 715, 833.
Parker, S., Kiyota, S., Morrell, N., et al. 2013, Central Bureau Electronic Telegrams, 3506, 1
Parker, S., Brimacombe, J., Marion, G. H., et al. 2014, Central Bureau Electronic Telegrams, 3905, 1
Parker, S., Arcavi, I., Hosseinzadeh, G., et al. 2015, Central Bureau Electronic Telegrams 4047, 1.
Pastorello, A., Valenti, S., Zampieri, L., et al. 2009, MNRAS, 394, 2266.
Patat, F., Barbon, R., Cappellaro, E., et al. 1993, A&AS, 98, 443.
Pessi, P. J., Folatelli, G., Anderson, J. P., et al. 2019, MNRAS, 1836
Phillips, M. M., Contreras, C., Hsiao, E. Y., et al. 2019, PASP, 131, 14001.
Podsiadlowski, P. 1992, PASP, 104, 717.
Popov, D. V. 1993, ApJ, 414, 712.
Pozzo, M., Meikle, W. P. S., Rayner, J. T., et al. 2006, MNRAS, 368, 1169.
Rank, D. M., Bregman, J., Witteborn, F. C., et al. 1988, ApJ, 325, L1.
Rayner, J. T., Toomey, D. W., Onaka, P. M., et al. 2003, PASP, 115, 362.
Rho, J., Geballe, T. R., Banerjee, D. P. K., et al. 2018, ApJL, 864, L20
Rodríguez, Ó., Pignata, G., Hamuy, M., et al. 2019, MNRAS, 483, 5459.
Rubin, A., & Gal-Yam, A. 2016, ApJ, 828, 111.
Sanders, N. E., Soderberg, A. M., Gezari, S., et al. 2015, ApJ, 799, 208.
Schlegel, E. M. 1990, MNRAS, 244, 269
Schwarz, G. 1978, Annals of Statistics, 6, 461.
Shappee, B. J., Stanek, K. Z., Kochanek, C. S., et al. 2013, The Astronomer's Telegram, 5665, 1.
Sharp, C. M., & Hoeflich, P. 1990, Ap&SS, 171, 213.
Shurpakov, S., Denisenko, D., Lipunov, V., et al. 2013, The Astronomer's Telegram, 5630, 1.
Shurpakov, S., Denisenko, D., Lipunov, V., et al. 2014, The Astronomer's Telegram, 6435, 1.
Silverman, B. W. 1981, J. Roy. Stat. Soc., Ser. B., Volume 43, p. 97-99, 43, 97
Simcoe, R. A., Burgasser, A. J., Schechter, P. L., et al. 2013, PASP, 125, 270.
Siviero, A., Tomasella, L., Pastorello, A., et al. 2012, Central Bureau Electronic Telegrams 3054, 4.
Smartt, S. J., Maund, J. R., Hendry, M. A., et al. 2004, Science, 303, 499.
Smartt, S. J. 2009, ARA&A, 47, 63.
Smartt, S. J. 2015, PASA, 32, e016.

Smith, D., Höflich, P., & Wheeler, J. C. 2001, Revista Mexicana De Astronomia Y Astrofisica Conference Series, 195.
Springob, C. M., Magoulas, C., Colless, M., et al. 2014, MNRAS, 445, 2677
Spyromilio, J., Meikle, W. P. S., Learner, R. C. M., et al. 1988, Nature, 334, 327.
Spyromilio, J., Leibundgut, B., & Gilmozzi, R. 2001, A&A, 376, 188.
Suzuki, N. 2006, ApJS, 163, 110.
Szalai, T., Vinkó, J., Könyves-Tóth, R., et al. 2019, ApJ, 876, 19.
Takáts, K., Pumo, M. L., Elias-Rosa, N., et al. 2014, MNRAS, 438, 368.
Takáts, K., Pignata, G., Pumo, M. L., et al. 2015, MNRAS, 450, 3137.
Takeda, Y. 1990, A&A, 234, 343
Tanaka, M., Phillips, M. M., Hsiao, E. Y., et al. 2014, Central Bureau Electronic Telegrams 3816, 1.
Tartaglia, L., Sand, D. J., Valenti, S., et al. 2018, ApJ, 853, 62
Terry, J. N., Paturel, G., & Ekholm, T. 2002, A&A, 393, 57
Tomasella, L., Cappellaro, E., Fraser, M., et al. 2013, MNRAS, 434, 1636.
Tully, R. B., & Fisher, J. R. 1988, Catalog of Nearby Galaxies.
Tully, R. B., Courtois, H. M., Dolphin, A. E., et al. 2013, AJ, 146, 86.
Vacca, W. D., Cushing, M. C., & Rayner, J. T. 2003, PASP, 115, 389
Valenti, S., Pastorello, A., Benitez-Herrera, S., et al. 2012, The Astronomer's Telegram, 4037, 1.
Valenti, S., Sand, D., Pastorello, A., et al. 2014, MNRAS, 438, L101.
Valenti, S., Sand, D., Stritzinger, M., et al. 2015, MNRAS, 448, 2608.
Valenti, S., Howell, D. A., Stritzinger, M. D., et al. 2016, MNRAS, 459, 3939.
Van Dyk, S. D. 2017, Handbook of Supernovae, 693.
Van Dyk, S. D., Zheng, W., Maund, J. R., et al. 2019, ApJ, 875, 136
Walker, E. S., Hadjiyska, E., Rabinowitz, D., et al. 2013, The Astronomer's Telegram, 5567, 1.
Whitelock, P. A., Catchpole, R. M., Menzies, J. W., et al. 1988, MNRAS, 234, 5P.
Woosley, S. E., & Iben, I. 1987, BAAS19, 1036.
Yaron, O., Perley, D. A., Gal-Yam, A., et al. 2017, Nature Physics, 13, 510.
Zheng, W., Blanchard, P., Cenko, S. B., et al. 2013, The Astronomer's Telegram, 4823, 1.
Zheng, W., Li, W., Filippenko, A. V., et al. 2013, The Astronomer's Telegram, 5563, 1.
Zheng, W., Li, W., Filippenko, A. V., et al. 2014, The Astronomer's Telegram, 5715, 1.
Zheng, W., Graham, M. L., Bigley, A., et al. 2015, The Astronomer's Telegram, 7143, 1.

Table 1. Supernovae in the Sample

Name	Type	s_2 (mag 100 day^{-1})	NIR Spectra	V-band Photometry	Discovery (YYYY-MM-DD)	Discovery (MJD)	Last Non-Detection (MJD)	Discovery Reference	Last Non-Detection Reference
ASASSN-13dn	II	-	1	No	2013-12-11.6	56637.6	56497.3	Shappee et al. (2013)	Shappee et al. (2013)
ASASSN-14gm	IIP	0.43 (0.36)	4	Yes	2014-09-02.5	56902.5	56899.5	Holoien et al. (2014)	Valenti et al. (2016)
ASASSN-14jb	IIP	-0.03 (0.14)	1	Yes	2014-10-19.1	56949.1	56943.0	Brimacombe et al. (2014)	Brimacombe et al. (2014)
ASASSN-15bb	IIP	0.47 (0.06)	5	Yes	2015-01-16.3	57038.3	57036.3	Kiyota et al. (2015)	Kiyota et al. (2015)
ASASSN-15fz	IIP	0.94 (0.19)	2	Yes	2015-03-30.6	57111.6	57110.3	Brimacombe et al. (2015)	Brimacombe et al. (2015)
ASASSN-15jp	II	-	1	Yes	2015-05-21.1	57163.1	57161.0	Holoien et al. (2015)	Holoien et al. (2015)
CATA13A	II	-	1	No	2013-12-07.2	56633.2	56415.9	Lyman et al. (2013)	Maza et al. (2013)
KISS14J	II	-	1	No	2014-02-23.5	56711.5	-	Tanaka et al. (2014)	-
LSQ12bri	II	-	1	No	2012-04-06	56023	-	Valenti et al. (2012)	-
LSQ12dcl	II	-	1	No	2012-06-24.4	56102.4	-	Hadjiyska et al. (2012)	-
LSQ13dpa	IIP	0.28 (2.01)	1	Yes	2013-12-18.3	56644.3	-	Hsiao et al. (2013)	-
LSQ15ok	IIP	1.03 (0.11)	1	Yes	2015-02-02	57069.6	57055	Mitra et al. (2015)	Zheng et al. (2015)
iPTF13dqy	II	-	1	No	2013-10-07.5	56572.5	56570.4	Nakano et al. (2013)	Yaron et al. (2017)
iPFT13dzb	II	-	1	No	2013-11-08	56604	-	Walker et al. (2013)	-
SN 2012A	IIP	0.94 (0.09)	1	Yes	2012-01-07.4	55933.4	55924	Moore et al. (2012)	Luppi et al. (2012)
SN 2012aw	IIP	1.27 (0.07)	5	Yes	2012-03-16.9	56002.9	56001.9	Siviero et al. (2012)	Dall'Ora et al. (2014)
SN 2012hs	II	-	1	No	2012-12-15.2	56276.2	56272.3	Cifuentes et al. (2012)	Cifuentes et al. (2012)
SN 2013ab	IIP	1.33 (0.01)	4	Yes	2013-02-17.5	56340.5	56338	Zheng et al. (2013)	Zheng et al. (2013)
SN 2013ai	IIL	1.61 (0.01)	1	Yes	2013-03-01.7	56352.7	56329.7	Conseil et al. (2013)	Conseil et al. (2013)
SN 2013by	IIL	2.8 (0.01)	3	Yes	2013-04-24.3	56406.3	-	Parker et al. (2013)	-
SN 2013ej	IIL	2.34 (0.79)	5	Yes	2013-07-25.5	56498.5	-	Kim et al. (2013)	-
SN 2013gd	IIP	0.64 (0.02)	12	Yes	2013-11-09.4	56605.4	56601	Zheng et al. (2013)	Zheng et al. (2013)
SN 2013gu	IIL	1.91 (0.04)	6	Yes	2013-12-05.8	56631.8	56212.9	Shurpakov et al. (2013)	Shurpakov et al. (2013)
SN 2013hj	IIL	1.59 (0.66)	14	Yes	2013-12-12.3	56638.3	-	Antezana et al. (2013)	-
SN 2013ht	II	-	1	No	2013-12-31.4	56657.4	-	Howerton et al. (2014)	-
SN 2014A	II	-	1	No	2014-01-01.6	56658.6	-	Zheng et al. (2014)	-
SN 2014bt	II	-	2	No	2014-05-31.6	56809.6	-	Parker et al. (2014)	-
SN 2014cw	IIP	0.54 (0.09)	1	Yes	2014-08-29.5	56898.5	56842.9	Shurpakov et al. (2014)	Shurpakov et al. (2014)
SN 2014cy	II	-	1	No	2014-08-31.7	56900.7	-	Nishimura (2014)	-
SN 2014dw	IIL	2.84 (0.07)	1	Yes	2014-11-6.6	56967.6	-	Parker et al. (2015)	-

NOTE—Some discovery and last non-detection observations were reported without time of day and thus are quoted here as such.

Table 2. Log of NIR observations

SN	UT Date	JD	Phase	Instrument	Telescope	S/N
ASASSN-13dn	2014-02-22	2456711	143.5	FIRE	Baade	113
ASASSN-14gm	2014-09-03	2456904	0.0	FIRE	Baade	129
	2014-09-23	2456924	21.0	SpeX	IRTF	99
	2014-12-14	2457006	102.0	FIRE	Baade	101
	2015-01-05	2457028	124.0	FIRE	Baade	35
ASASSN-14jb	2014-11-05	2456967	20.0	FIRE	Baade	111
ASASSN-15bb	2015-01-28	2457051	13.8	FIRE	Baade	375
	2015-03-07	2457089	51.8	FIRE	Baade	109
	2015-04-07	2457120	82.8	FIRE	Baade	109
	2015-04-12	2457125	87.8	FIRE	Baade	53
	2015-06-02	2457176	138.8	FIRE	Baade	43
ASASSN-15fz	2015-04-02	2457115	4.0	FIRE	Baade	142
	2015-04-07	2457120	9.0	FIRE	Baade	155
ASASSN-15jp	2015-06-02	2457176	14.0	FIRE	Baade	310
CATA13A	2013-12-09	2456636	111.5	FIRE	Baade	71
KISS14J	2014-02-27	2456716	15.5	FIRE	Baade	44
LSQ12bri	2012-04-08	2456026	3.0	FIRE	Baade	107
LSQ12dcl	2012-06-26	2456105	2.5	FIRE	Baade	69
LSQ13dpa	2013-12-20	2456647	4.8	FIRE	Baade	60
LSQ15ok	2015-03-07	2457089	17.0	FIRE	Baade	102
iPTF13dqy	2013-11-14	2456611	39.5	FIRE	Baade	69
iPTF13dzb	2013-11-20	2456617	13.0	FIRE	Baade	54
SN 2012A	2012-01-15	2455942	13.2	FIRE	Baade	589
SN 2012aw	2012-04-08	2456026	23.5	FIRE	Baade	155
	2012-04-11	2456029	26.5	FIRE	Baade	259
	2012-04-19	2456037	34.5	FIRE	Baade	173
	2012-04-30	2456048	45.5	FIRE	Baade	135
	2012-05-07	2456055	52.5	FIRE	Baade	124
SN 2012hs	2013-01-06	2456299	24.8	FIRE	Baade	56
SN 2013ab	2013-02-28	2456352	12.8	FIRE	Baade	172
	2013-03-20	2456372	32.8	FIRE	Baade	186
	2013-05-19	2456432	92.8	FIRE	Baade	92
SN 2013ai	2013-03-20	2456372	24.0	FIRE	Baade	150
SN 2013by	2013-04-24	2456407	3.0	FIRE	Baade	318
	2013-05-22	2456435	31.0	FIRE	Baade	121
	2013-07-29	2456503	99.0	FIRE	Baade	54
SN 2013ej	2013-07-29	2456503	5.8	FIRE	Baade	573
	2013-09-11	2456547	49.8	SpeX	IRTF	231
	2013-10-25	2456591	93.8	FIRE	Baade	50

Table 2 continued

Table 2 *(continued)*

SN	UT Date	JD	Phase	Instrument	Telescope	S/N
	2013-11-14	2456611	113.8	FIRE	Baade	29
	2013-12-14	2456641	143.8	FIRE	Baade	96
SN 2013gd	2013-11-14	2456611	7.8	FIRE	Baade	105
	2013-11-30	2456627	23.8	FIRE	Baade	283
	2013-12-09	2456636	32.8	FIRE	Baade	102
	2013-12-14	2456641	37.8	FIRE	Baade	110
	2013-12-20	2456647	43.8	FIRE	Baade	139
	2013-12-27	2456654	50.8	FIRE	Baade	57
	2014-01-01	2456659	55.8	FIRE	Baade	182
	2014-01-09	2456667	63.8	FIRE	Baade	76
	2014-01-14	2456672	68.8	FIRE	Baade	41
	2014-02-08	2456697	93.8	FIRE	Baade	45
	2014-02-27	2456716	112.8	FIRE	Baade	68
	2014-03-18	2456735	131.8	FIRE	Baade	27
SN 2013gu	2013-12-09	2456636	3.5	FIRE	Baade	234
	2013-12-14	2456641	8.5	FIRE	Baade	90
	2013-12-20	2456647	14.5	FIRE	Baade	96
	2013-12-27	2456654	21.5	FIRE	Baade	84
	2014-01-09	2456667	34.5	FIRE	Baade	68
	2014-01-14	2456672	39.5	FIRE	Baade	42
SN 2013hj	2013-12-14	2456641	4.0	FIRE	Baade	305
	2013-12-20	2456647	10.0	FIRE	Baade	366
	2013-12-27	2456654	17.0	FIRE	Baade	219
	2014-01-01	2456659	22.0	FIRE	Baade	205
	2014-01-09	2456667	30.0	FIRE	Baade	93
	2014-02-08	2456697	60.0	FIRE	Baade	267
	2014-02-15	2456704	67.0	FIRE	Baade	107
	2014-02-22	2456711	74.0	FIRE	Baade	161
	2014-02-27	2456716	79.0	FIRE	Baade	95
	2014-03-10	2456727	90.0	FIRE	Baade	154
	2014-03-25	2456742	105.0	FIRE	Baade	64
	2014-04-23	2456771	134.0	FIRE	Baade	39
SN 2013ht	2014-01-01	2456659	1.5	FIRE	Baade	62
SN 2014A	2014-01-02	2456660	45.5	FIRE	Baade	77
SN 2014bt	2014-06-06	2456815	5.5	FIRE	Baade	226
	2014-07-10	2456849	39.5	FIRE	Baade	334
SN 2014cw	2014-09-03	2456904	33.2	FIRE	Baade	130
SN 2014cy	2014-09-03	2456904	12.0	FIRE	Baade	119
SN 2014dw	2014-12-14	2457006	38.5	FIRE	Baade	65

Table 3. Supernova Host Galaxies

Name	Redshift	RA	Dec	Host Galaxy
ASASSN-13dn	0.023	12:52:58.39	+32:25:05.60	SDSS J125258.03+322444.3
ASASSN-14gm	0.006	00:59:47.83	−07:34:19.30	NGC 337
ASASSN-14jb	0.006	22:23:16.12	−28:58:30.78	ESO 467-G051
ASASSN-15bb	0.016	13:01:06.38	−36:36:00.17	ESO 381-IG048
ASASSN-15fz	0.017	13:35:25.14	+01:24:33.00	NGC 5227
ASASSN-15jp	0.010	10:11:38.99	−31:39:04.04	NGC 3157
CATA13A	0.035	06:25:10.07	−37:20:41.30	ESO 365-G16
KISS14J	0.018	11:14:52.16	+19:27:17.80	NGC 3859
LSQ12bri	0.030	13:35:48.35	−21:23:53.47	Unknown
LSQ12dcl	0.031	00:13:43.35	−00:27:58.38	SDSS J001343.81-002735.7
LSQ13dpa	0.024	11:01:12.91	−5:50:52.57	LCSB S1492O
LSQ15ok	0.014	10:49:16.67	−19:38:26.01	ESO 569-G12
iPTF13dqy	0.012	23:19:44.70	+10:11:04.40	NGC 7610
iPFT13dzb	0.037	03:10:50.20	−00:21:40.30	2MASX J03104933-0021256
SN 2012A	0.003	10:25:07.38	+17:09:14.60	NGC 3239
SN 2012aw	0.003	10:43:53.72	+11:40:17.70	M95
SN 2012hs	0.006	09:49:14.71	−47:54:45.60	ESO 213-2
SN 2013ab	0.005	14:32:44.49	+09:53:12.30	NGC 5669
SN 2013ai	0.009	06:16:18.35	−21:22:32.90	NGC 2207
SN 2013by	0.004	16:59:02.43	−60:11:41.80	ESO 138-G10
SN 2013ej	0.002	01:36:48.16	+15:45:31.00	M74
SN 2013gd	0.013	03:49:05.64	−03:03:28.30	MCG-01-10-039
SN 2013gu	0.018	01:46:38.27	+04:13:24.40	SDSS J014638.24+041333.3
SN 2013hj	0.007	09:12:06.29	−15:25:46.00	MCG -02-24-003
SN 2013ht	0.028	10:55:50.95	−09:51:42.40	MCG -02-28-21
SN 2014A	0.006	13:16:59.36	−16:37:57.00	NGC 5054
SN 2014bt	0.016	21:43:11.13	−38:58:05.80	IC 5128
SN 2014cw	0.009	22:15:26.55	−10:28:34.60	PGC 68414
SN 2014cy	0.006	23:44:16.03	+10:46:12.50	NGC 7742
SN 2014dw	0.008	11:10:48.41	−37:27:02.20	NGC 3568

APPENDIX

A. LIGHT CURVES

For early epochs and plateau phase, a four-parameter fit is applied to determine the decline rates (s_1 and s_2), the transition epoch between the two decline rates ($t_{\rm trans}$), and the magnitude offset of the light curve. Fitting is also performed with multiple linear three parameter functions in order to determine if the light curve has two distinct early time decline phases characterized by multiple slopes. Bayesian Information Criterion (Schwarz 1978) was used to determine the goodness of fit between the three and four-parameter models. A linear fit is also applied to determine the radioactive decay tail slope, s_3, if sufficient photometric data past the plateau exists. The midpoint time of transition, $t_{\rm PT}$ between the plateau and linear decline phases is obtained through fitting the light curves with an eight-parameter fit function from Olivares E. et al. (2010),

$$F(t) = \frac{-a_0}{1 + e^{(t-t_{PT})/w_0}} + p_0(t - t_{PT}) + m_0 - Pe^{-(\frac{t-Q}{R})^2}, \tag{A1}$$

Table 4. Supernova Distances

SN	Redshift Distance Modulus	Redshift Independent Distance Modulus	Method	Reference
ASASSN-13dn	34.98 (0.09)	-	-	-
ASASSN-14gm	31.63 (0.43)	31.38 (0.20)	Tully-Fisher	Tully et al. (2013)
ASASSN-14jb	32.03 (0.36)	30.89 (0.32)	Tully-Fisher	Mathewson et al. (1992)
ASASSN-15bb	34.18 (0.14)	-	-	-
ASASSN-15fz	34.31 (0.13)	-	-	-
ASASSN-15jp	32.91 (0.24)	33.26 (0.13)	Tully-Fisher	Springob et al. (2014)
CATA13A	35.91 (0.06)	-	-	-
KISS14J	34.43 (0.12)	35.03 (0.08)	Tully-Fisher	Springob et al. (2014)
LSQ12bri	35.56 (0.07)	-	-	-
LSQ12dcl	35.64 (0.07)	-	-	-
LSQ13dpa	34.98 (0.09)	-	-	-
LSQ15ok	33.88 (0.16)	-	-	-
iPTF13dqy	33.54 (0.18)	33.51 (0.10)	Tully-Fisher	Springob et al. (2014)
iPFT13dzb	36.03 (0.06)	37.35 (0.94)	FP	Springob et al. (2014)
SN 2012A	30.52 (0.72)	-	-	-
SN 2012aw	30.00 (0.09)	30.10 (0.06)	Cepheids	Freedman et al. (2001)
SN 2012hs	32.03 (0.36)	-	-	-
SN 2013ab	31.63 (0.43)	-	-	-
SN 2013ai	32.91 (0.24)	32.99 (0.30)	SNIa	Arnett (1982)
SN 2013by	31.15 (0.54)	30.84 (0.80)	Tully-Fisher	Tully, & Fisher (1988)
SN 2013ej	29.64 (1.09)	30.04 (0.03)	TRGB	Jang, & Lee (2014)
SN 2013gd	33.72 (0.17)	-	-	-
SN 2013gu	34.43 (0.12)	-	-	-
SN 2013hj	32.37 (0.31)	31.94 (0.80)	Tully-Fisher	Makarov et al. (2014)
SN 2013ht	35.41 (0.07)	-	-	-
SN 2014A	32.03 (0.36)	31.30 (0.20)	Tully-Fisher	Tully et al. (2013)
SN 2014bt	34.15 (0.14)	-	-	-
SN 2014cw	32.91 (0.24)	-	-	-
SN 2014cy	32.03 (0.36)	31.73 (0.80)	Tully-Fisher	Tully, & Fisher (1988)
SN 2014dw	32.66 (0.27)	32.63 (0.10)	Sosies	Terry et al. (2002)

Note—Assuming $H_0 = 71, \Omega_m = 0.27, \Omega = 0.73$, and that each has a peculiar velocity of 300 km s^{-1}. The distance modulus error is given in parenthesis.

where t_{PT} corresponds to the midpoint of transition between plateau and radioactive tail, and m_0 is the zero point magnitude at the transition time. The first term is a Fermi-Dirac function that describes the transition between plateau and linear decline phases. The second term and zero point magnitude, m_0, describe the radioactive tail of the light curve and offset the fit, respectively. The last term is a Gaussian that describes the shape of the light curve during the plateau. Figures A.2 and A.3 show the CSP-II V-band light curves, as well as other light curves from the literature. Results of the fitting are listed in Table A.1.

Table 5. Previously published supernova classifications.

Name	Photometric Classification	s_2 (mag 100 days^{-1})	NIR Spectroscopic Classification	Publication
SN 1997D	-	-	Weak	Benetti et al. (2001)
SN 1999em	IIP	0.37 (0.02)	-	Hamuy et al. (2001), Elmhamdi et al. (2003)
SN 2002hh	IIP	0.73 (0.18)	-	Pozzo et al. (2006)
SN 2004et	IIP	0.93 (0.15)	-	Maguire et al. (2010)
SN 2005cs	IIP	0.43 (0.12)	Weak	Pastorello et al. (2009)
SN 2008in	IIP	0.89 (0.03)	Weak	Takáts et al. (2014)
SN 2009N	IIP	0.90 (0.22)	Weak	Takáts et al. (2014)
SN 2009ib	IIP	0.27 (0.07)	Weak	Takáts et al. (2015)
SN 2009md	IIP	-	Weak	Fraser et al. (2011)
SN 2012A	IIP	0.94 (0.09)	Strong	Tomasella et al. (2013)
SN 2012aw	IIP	1.27 (0.07)	Weak	Dall'Ora et al. (2014), Jerkstrand et al. (2014)
SN 2013by	IIL	2.80 (0.01)	Strong	Valenti et al. (2015)
SN 2013ej	IIL	2.34 (0.79)	Strong	Valenti et al. (2014)
ASASSN-15oz	IIL	-	Strong	Bostroem et al. (2019)
SN 2016ija	IIL	2.39 (0.38)	Strong	Tartaglia et al. (2018)
SN 2017eaw	IIP	0.74 (0.15)	Weak	Rho et al. (2018)
SN 2017gmr	IIP	-	Weak	Andrews et al. (2019)

NOTE—SN 2008in, SN 2009md, and SN 2012A were spectroscopically classified based on the features present in their published spectra, not a pEW measurement, as their data is not publicly accessible. A value of s_2 cannot be measured for SN 2009md and ASASSN-15oz as they have no publicly available photometry, thus their photometric classification is taken from their respective publications. SN 1997D has sparse photometric coverage and an uncertain explosion date so no value of s_2 can be measured.

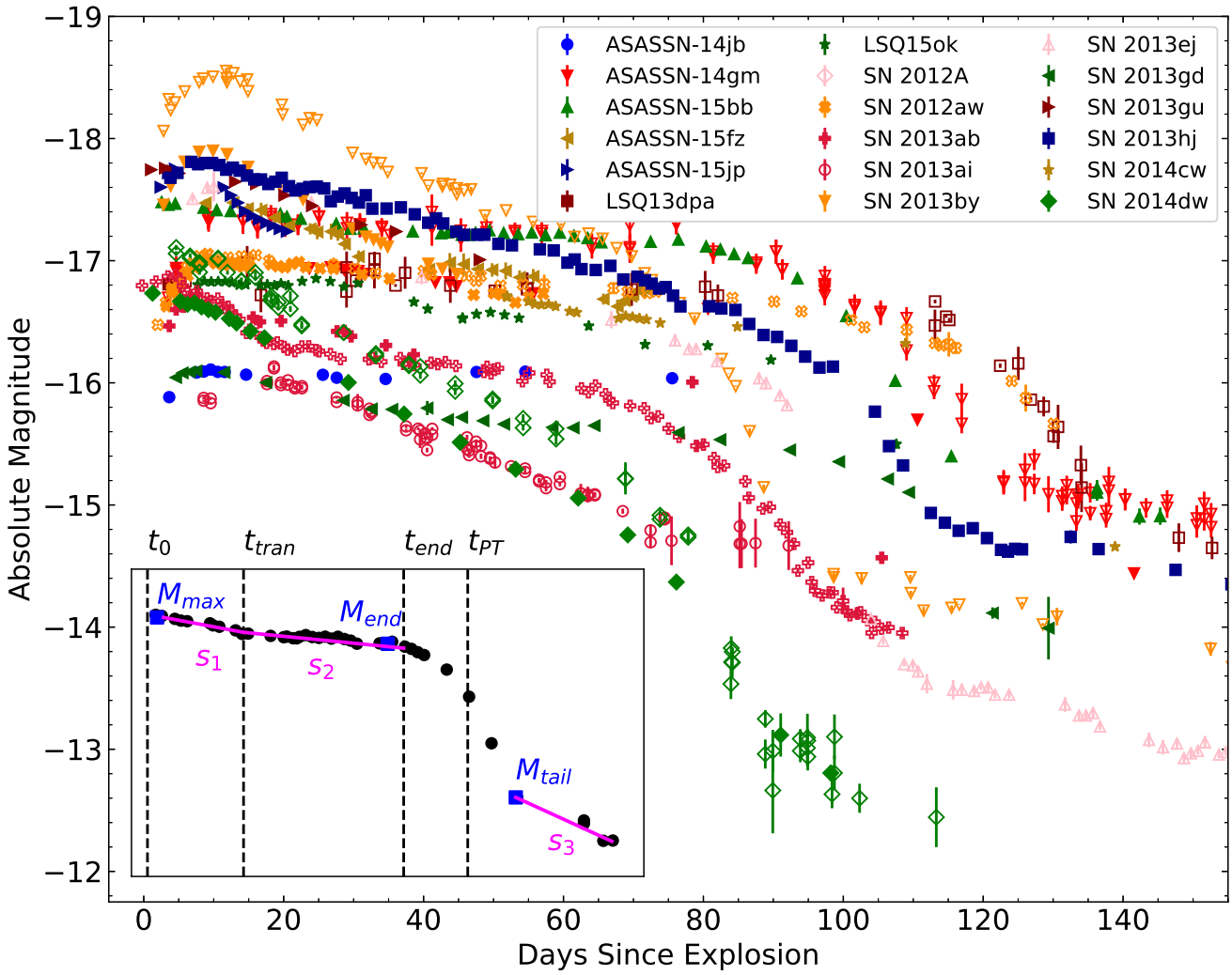

Figure A.1. All Milky Way extinction corrected V-band light curve data plotted together in absolute magnitude. Errors are shown for each data point, unless smaller than the symbol. Open symbols represent data gathered from previously published work. The inset shows an example light fit with the parameters outlined in the text.

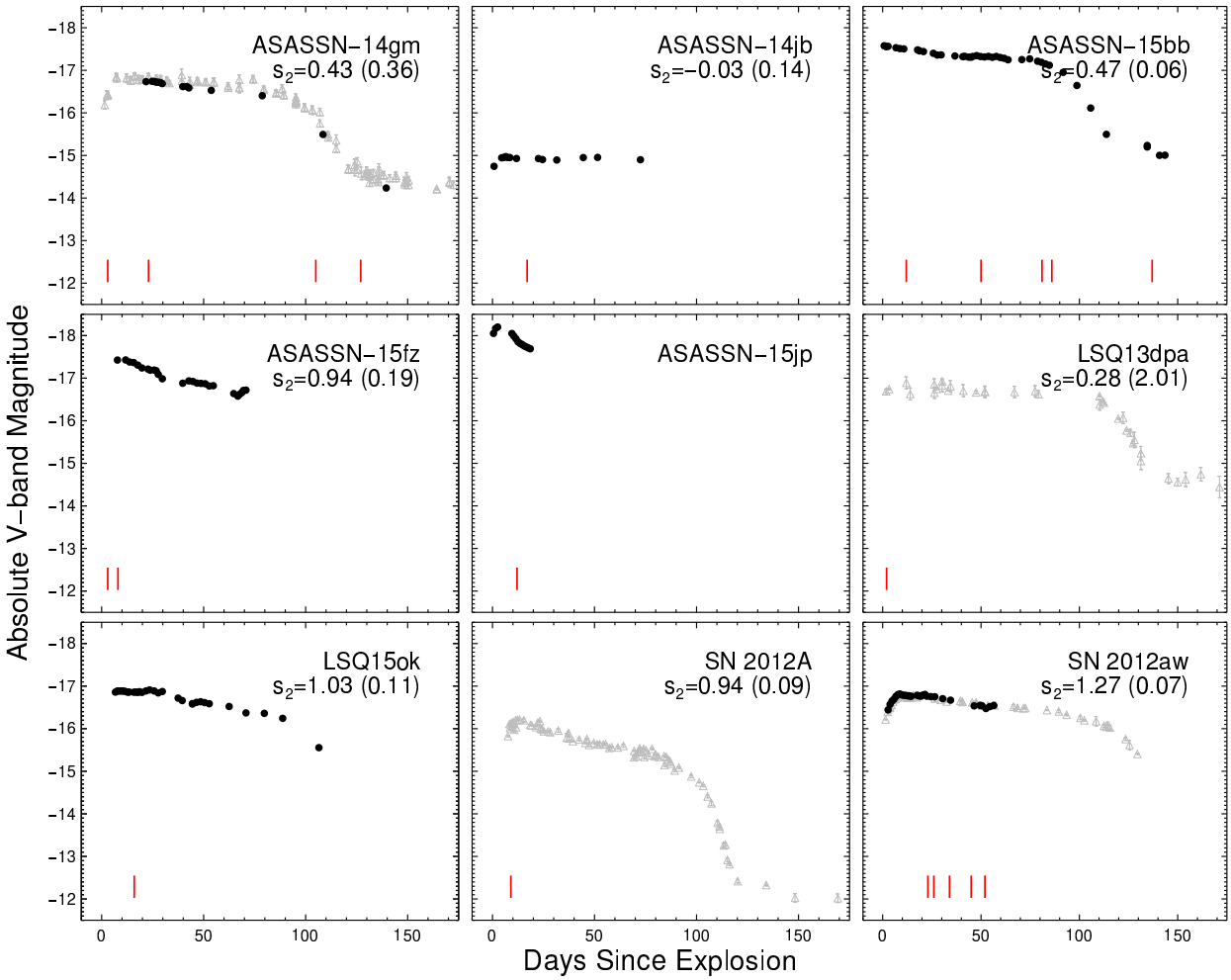

Figure A.2. Milky Way extinction corrected V-band light curves that were measured. Black dots are data from CSP-II, and grey triangles represent previously published data. Red ticks at the bottom of each panel represent the epoch of NIR spectra taken. The optical data is taken from previously published data.

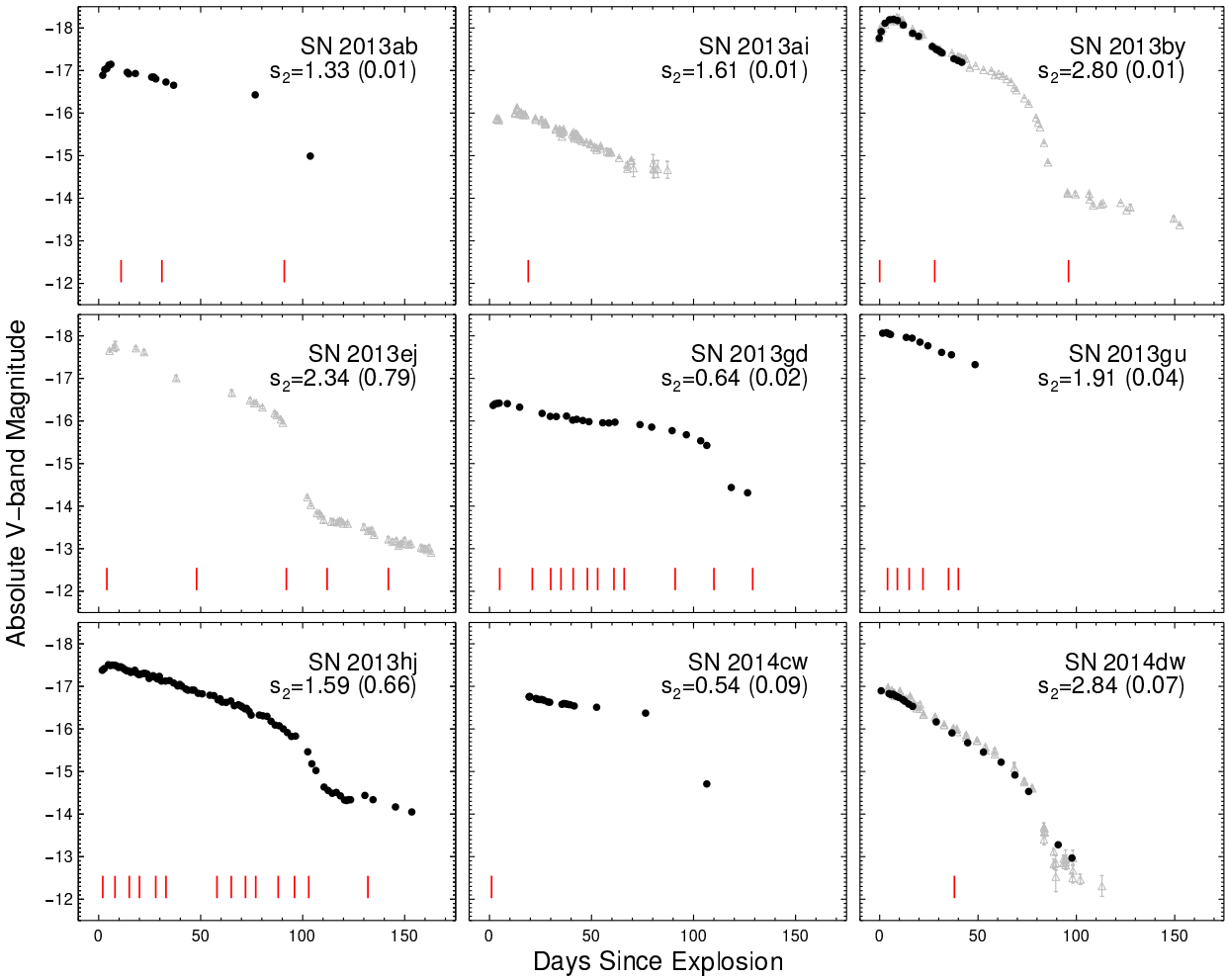

Figure A.3. Figure A.2 continued.

Table A.1. V-band light curve measurements

SN	s_1 (mag 100 day^{-1})	s_2 (mag 100 day^{-1})	s_3 (mag 100 day^{-1})	$M_{\rm max}$ (mag)	$M_{\rm end}$ (mag)	$M_{\rm tail}$ (mag)	$t_{\rm tran}$ (mag)	$t_{\rm end}$ (days)	$t_{\rm PT}$ (days)	Pd ($t_{\rm end} - t_{\rm tran}$) (days)	OPTd ($t_{\rm end} - t_0$) (days)
ASASSN-14gm	0.43 (0.36)	0.43 (0.36)	0.77 (0.02)	−16.87 (0.01)	−16.54 (0.07)	−14.47 (0.05)	-	43.25 (10.36)	110.93 (0.12)	-	43.25 (10.36)
ASASSN-14jb	0.25 (0.14)	−0.03 (0.14)	-	−14.93 (0.01)	-	-	31.50 (19.7)	-	-	-	-
ASASSN-15bb	0.60 (0.130)	0.47 (0.06)	2.65 (1.22)	−17.52 (0.01)	−17.27 (0.02)	−15.23 (0.02)	45.75 (11.1)	84.75 (0.0)	104.82 (0.29)	39.00 (11.1)	84.75 (0.01)
ASASSN-15fz	2.02 (0.46)	0.94 (0.19)	-	−18.03 (0.02)	-	-	39.75 (14.3)	-	-	-	-
ASASSN-15jp	2.97 (0.07)	-	-	−18.216 (0.02)	-	-	-	-	-	-	-
LSQ13dpa	0.28 (2.01)	0.28 (2.01)	0.68 (1.65)	−16.69 (0.01)	−16.33 (0.17)	−14.57 (0.17)	-	115.00 (29.31)	128.46 (0.47)	-	115.00 (29.31)
LSQ15ok	1.03 (0.66)	1.03 (0.11)	-	−16.93 (0.01)	−15.55 (0.07)	-	-	88.75 (8.05)	-	-	88.75 (8.05)
SN 2012A	1.74 (0.47)	0.94 (0.09)	1.04 (0.28)	−16.14 (0.01)	−15.39 (0.03)	−12.33 (0.02)	45.47 (13.18)	87.11 (25.67)	109.87 (0.12)	41.64 (15.84)	87.11 (25.67)
SN 2012aw	1.27 (0.07)	1.27 (0.07)	-	−16.72 (0.01)	-	-	-	-	-	-	-
SN 2013ab	1.33 (0.01)	1.33 (0.01)	-	−17.05 (0.01)	-	-	-	-	-	-	-
SN 2013ai	1.61 (0.01)	1.61 (0.01)	-	−15.9 6(0.01)	-	-	-	-	-	-	-
SN 2013by	2.80 (0.01)	2.80 (0.01)	1.20 (0.03)	−18.35 (0.01)	−17.01 (0.01)	−13.85 (0.01)	-	21.75 (0.01)	82.58 (0.03)	-	21.75 (0.01)
SN 2013ej	2.34 (0.79)	2.34 (0.79)	1.58 (0.08)	−17.74 (0.14)	−16.66 (2.31)	−12.43 (0.04)	-	65.25 (24.92)	95.8741 (0.277419)	-	65.25 (24.92)
SN 2013gd	1.25 (0.17)	0.64 (0.02)	-	−16.38 (0.01)	−15.85 (0.03)	-	32.75 (2.88)	103.50 (0.01)	111.93 (1.79)	70.75 (2.88)	103.50 (0.01)
SN 2013gu	0.94 (0.17)	1.91 (0.04)	-	−17.83 (0.01)	-	-	16.50 (2.19)	-	-	-	-
SN 2013hj	1.13 (0.13)	1.59 (0.66)	1.07 (0.08)	−17.86 (0.08)	−16.79 (0.06)	−14.48 (0.07)	26.11 (18.74)	82.50 (2.09)	103.17 (2.71)	56.39 (16.7)	82.50 (2.09)
SN 2014cw	1.35 (0.30)	0.54 (0.09)	-	−16.75 (0.01)	-	-	29.50 (5.50)	-	-	-	-
SN 2014dw	2.37 (0.15)	2.84 (0.07)	-	−17.01 (0.01)	-	-	17.75 (3.83)	68.50 (0.01)	-	50.75 (3.83)	68.50 (0.01)